Report No. NADC-88141-60 (Volume II)

DTIC
S ELECTE
MAY 26 1989
D

AD-A208 346

RESIDUAL STRESS CHANGES
IN FATIGUE
VOLUME II — A SIMULATION MODEL
FOR STRESS MEASUREMENTS IN NOTCH_D
TEST SPECIMENS BY X-RAY DIFFRACTION

K. Ranganathan
Engineering Science and Mechanics Department
VIRGINIA POLYTECHNIC INSTITUTE AND STATE UNIVERSITY
Blacksburg, VA 24061

Prepared for
Air Vehicles and Crew Systems Technology Department (Code 6043)
NAVAL AIR DEVELOPMENT CENTER
Warminster, PA 18974-5000

NOTICES

REPORT NUMBERING SYSTEM - The numbering of technical project reports issued by the Naval Air Development Center is arranged for specific identification purposes. Each number consists of the Center acronym, the calendar year in which the number was assigned, the sequence number of the report within the specific calandar year, and the official 2-digit correspondence code of the Command Officer or the Functional Department responsible for the report. For example: Report No. NADC 88020-60 indicates the twentieth Center report for the year 1988 and prepared by the Air Vehicle and Crew Systems Technology Department. The numerical codes are as follows:

CODE	OFFICE OR DEPARTMENT
00	Commander, Naval Air Development Center
01	Technical Director, Naval Air Development Center
05	Computer Department
10	AntiSubmarine Warfare Systems Department
20	Tactical Air Systems Department
30	Warfare Systems Analysis Department
40	Communication Navigation Technology Department
50	Mission Avionics Technology Department
60	Air Vehicle & Crew Systems Technology Department
70	Systems & Software Technology Department
80	Engineering Support Group
90	Test & Evaluation Group

REPORT DOCUMENTATION PAGE

Form Approved
OMB No 0704-0188

1a REPORT SECURITY CLASSIFICATION UNCLASSIFIED	1b RESTRICTIVE MARKINGS

2a SECURITY CLASSIFICATION AUTHORITY	3 DISTRIBUTION / AVAILABILITY OF REPORT
2b DECLASSIFICATION / DOWNGRADING SCHEDULE	Approved for Public Release; Distribution is Unlimited

4 PERFORMING ORGANIZATION REPORT NUMBER(S)	5 MONITORING ORGANIZATION REPORT NUMBER(S) NADC-88141-60 (Vol. II)

6a NAME OF PERFORMING ORGANIZATION Virginia Polytechnic Institute and State University	6b OFFICE SYMBOL (If applicable)	7a NAME OF MONITORING ORGANIZATION Air Vehicle & Crew Systems Technology Department (Code 6043) NAVAL AIR DEVELOPMENT CENTER
6c ADDRESS (City, State, and ZIP Code) Blacksburg, VA 24061		7b ADDRESS (City, State, and ZIP Code) Warminster, PA 18974

8a NAME OF FUNDING / SPONSORING ORGANIZATION NAVAL AIR SYSTEMS COMMAND	8b OFFICE SYMBOL (If applicable) AIR-931B	9 PROCUREMENT INSTRUMENT IDENTIFICATION NUMBER N62269-85-C-0256

8c ADDRESS (City, State, and ZIP Code) Department of the NAVY Washington, DC 20361	10 SOURCE OF FUNDING NUMBERS			
	PROGRAM ELEMENT NO 61153N	PROJECT NO	TASK NO R02303001	WORK UNIT ACCESSION NO 106362

11 TITLE (Include Security Classification)

(v) Residual Stress Changes in Fatigue: Vol. II, A Simulation Model for Stress Measurements in Notched Test Specimens by X-Ray Diffraction

12 PERSONAL AUTHOR(S)

Ranganathan, K.

13a TYPE OF REPORT Interim	13b TIME COVERED FROM Oct. 85 TO Sept. 87	14 DATE OF REPORT (Year, Month Day) 1989 March 1	15 PAGE COUNT 100

16 SUPPLEMENTARY NOTATION

This report consists of two volumes

17 COSATI CODES			18 SUBJECT TERMS (Continue on reverse if necessary and identify block number)
FIELD	GROUP	SUB-GROUP	Airframes; Fatigue (Mechanics); Fatigue Life; Predictions; Failure (Mechanics); Spectra. Computerized Simulation; Residual Stress; X-Ray Diffraction
01	03		
20	11		

19 ABSTRACT (Continue on reverse if necessary and identify by block number)

The state of stress developed during fatigue testing of notched tensile specimens was modeled analytically. From this model, the X-ray response to the stress state of the specimen was determined with an aim of measuring the X-ray effects that result from residual stresses. This model was also used to estimate the error in stress measurements caused by a stress gradient. The error in the measured stresses caused by the varying radius of curvature of the test specimen was also studied. It was concluded that the stress distribution model for an infinite specimen can be extended to a specimen of finite geometry with an error of approximately 3 percent, that precision in positioning the X-ray beam on the specimen is very important; and that residual stress measurements are feasible along the edge of the specimen.

20 DISTRIBUTION / AVAILABILITY OF ABSTRACT ☒ UNCLASSIFIED/UNLIMITED ☐ SAME AS RPT ☐ DTIC USERS	21 ABSTRACT SECURITY CLASSIFICATION UNCLASSIFIED
22a NAME OF RESPONSIBLE INDIVIDUAL R.E. Vining	22b TELEPHONE (Include Area Code) (215) 441-2730	22c OFFICE SYMBOL 6043

DD Form 1473, JUN 86   Previous editions are obsolete

S/N 0102-LF-014-6603

CONTENTS

THIS PAGE INTENTIONALLY LEFT BLANK

List of Illustrations

List of Illustrations (Continued)

List of Tables

FOREWORD

The work described in this report was performed by the Virginia Polytechnic

Institute and State University, Engineering Science and Mechanics Department, for the

Naval Air Development Center under contract number N62269-85-C-0256. The principal

investigator was Prof. Norman E. Dowling. DeRome O. Dunn, Graduate Research

Assistant, performed important portions of the work. Volume II was taken from a M. S.

thesis written by K. Ranganathan. The program manager for NADC was L. W. Gause.

the project engineer was R.E.Vining. This interim report covers

work that was performed during the time period October 1985 to December 1987.

1.0 Introduction

Fatigue crack initiation is a problem which causes considerable concern since it occurs in many materials. Most fractures in machine parts are a result of fatigue cracking. Fatigue failures are particularly insidious as they occur at nominal or average stresses which are well below the yield strength of the material and hence do not result in any visible signs of yielding in the material. Failure by fatigue begins with the initiation of a minute crack at a localized spot, usually at a stress concentration point, and gradually propagates through the section of an engineering component until the member breaks.

One aspect of material behaviour which can exert a significant influence on the fatigue life, but has not been adequately modelled, is the relaxation of the residual stresses present in the material. Such relaxation may be cycle or time dependent. A number of methods, both destructive and non-destructive, are available for measuring residual stresses. Hole drilling and ring coring are methods that are destructive in nature. Some non-destructive techniques used for measuring residual stresses include acoustic emission, ultrasonic, x-ray diffraction and the Barkhausen noise analysis technique

Various x-ray diffraction methods have been used in the past for different applications. However, measurements have yet to be made on test specimens mounted in a testing machine. Measuring time is crucial in applications which require the study of time dependent relaxation of residual stresses.

Experiments designed to study the time dependent relaxation of residual stresses are being conducted by other investigators in the laboratory on specimens containing stress raisers. These tests are being done on notched tensile specimens subjected to fatigue loading.

The objective of the present work was to analytically model the state of stresses developed during fatigue testing of notched tensile specimens. From this model, the x-ray response to the stress state of the specimen was determined with an aim of measuring the x-ray effects that result from residual stresses.

This model was developed in two parts. In the first part, a model for the stress distribution on the flat or plane surface of a notched specimen was developed for the region between the notches. The corresponding strain distribution was then calculated from Hooke's law of elasticity. These calculations were done for a specimen with a geometry similar to that used in experimental work. This model simulates the stress state which develops in a notched tensile specimen during experimental testing.

In the second part, the x-ray response from the strain distribution was first determined from the variation of d, the lattice spacing, with the angle ψ. This variation is illustrated as plots of d vs $\sin^2\psi$. Here, ψ is the angle between the diffraction vector (which is the bisector of the incident beam and the diffracted beam) and the normal to the sample. This is depicted in Figure 1. The second aspect studied in this model was the relationship between the stress gradient and the depth of penetration of the x-ray beam. This study was useful in estimating the error involved in the stress measurements due to the stress gradient. In addition, an estimate of the error in the stress values due to varying radius of curvature was also studied.

An important part of this simulation was the determination of the x-ray effects of the stress state in the specimen. This information was obtained in the form of line profiles. These profiles were simulated for the individual grains on the flat surface of the specimen in the region between the notches using a finite beam size. This simulation was useful in the study of the effects of the strain gradient in a specimen and therefore of a non-uniform macrostrain. The theory and results of this simulation are discussed in the last section.

THIS PAGE INTENTIONALLY LEFT BLANK

2.0 Literature Review

The role of residual stresses in the premature failure of metallic components has been recognized for a long time. There is a great need for the measurement of these stresses for a number o.˜ reasons. These include stringent quality specifications, the reduction of load safety margins, and the e˙olving application of fracture mechanics calculations. Two of the most prevalent methods [1] used ˜r the measurement of these stresses are hole drilling and ring coring. These two methods are sei.˜de-structive, as they disturb or remove material from the component, and may therefore degrade its serviceability. The methodologies of measurement and the difficulties associated with the destruc-tive techniques necessitates the use of non-destructive techniques for the measurement of residual stresses.

Numerous non-destructive techniques have been used for measuring stresses. Some of these meth-ods are - x-ray diffraction [6], ultrasonic [2] and Barkhausen noise analysis [3]. Of all these tech-niques, x-ray diffraction is the only non-destructive technique which is generally reliable and promising for a wide field of applications.

X-ray diffraction was first used by Lester and Aborn [4] in (1925-1926). The diffracted beams, in those days, were recorded on photographic films. In spite of the great advantage of being nonde-structive, x-ray diffraction has not been used widely, until recently. This was due to the excessive measurement time and the limitations on the size of the part on which measurement was to be done (maximum size of the order of a few centimeters). Today, x-ray diffraction is widely used due to the advancements made in both its theoretical and technological aspects.

2.1 Residual stresses

Residual stresses are defined as stresses which remain in a material after all applied forces are re-moved. Considering a material with a crystallographic grain structure, such as metals and alloys, residual stresses may be classified conventionally into three types. The first are stresses acting over dimensions of the order of a few grains. These stresses are long range in nature and may be termed macro-stresses. Macro-stresses may develop from mechanical, thermal and chemical processes. The second kind of stresses act over the dimension of a single grain and are termed micro-stresses. Micro-stresses may result from a difference in the mechanical properties of the different phases in a material. They are manifest as localized elastic expansion or contraction of the metal lattice may occur as a consequence of processes like nitriding, carburizing or phase transformations. The third kind of stresses range over a few inter-atomic distances. These stresses arise from the varying stress fields of individual dislocations, dislocation pileups, kink boundaries, and other microstructural phenomena which are of a discontinuous nature. The macro and the micro-stresses are measurable quantitatively by x-ray diffraction techniques. They may be detected separately by x-ray diffraction methods, if the total strains from all phases of a multiphase solid can be measured. The volume fraction of all the phases should also be measured.

Surface residual stresses exert a significant influence on the life of a material and occur at notches and scratches. Furthermore, such surface defects which concentrate additional stresses near the surface can act to initiate a crack. Compressive residual stresses in the surface are beneficial to components prone to fatigue failure or stress corrosion cracking, as these stresses have to be overcome by the applied load before cracks are initiated. On the other hand, residual tensile stresses are usually harmful and can be a major cause of brittle fracture, especially in fatigue. Consequently, the measurement of residual stresses is of considerable importance in determining the load carrying capabilities of the material.

2.2   X-ray diffraction

The principle of residual stress measurements by x-ray diffraction is based on the fact that when a polycrystalline metal or ceramic material is placed under stress, the elastic strains in the material are manifest as a change in the lattice spacings of its grains. The stress, be it externally applied or residual in the material, is taken up by the interatomic spacings. X-ray diffraction techniques can actually measure these interatomic spacings which are indicative of the macro elastic strain in the specimen. The corresponding stress values are obtained from these elastic strains from elastic stress-strain relationships. In applying these relationships, the material is assumed to be isotropic and homogenous in all of the volume irradiated by the x-rays.

Monochromatic x-ray radiation diffracts according to Bragg's law

$$n\lambda = 2d\sin\theta \qquad (2.01)$$
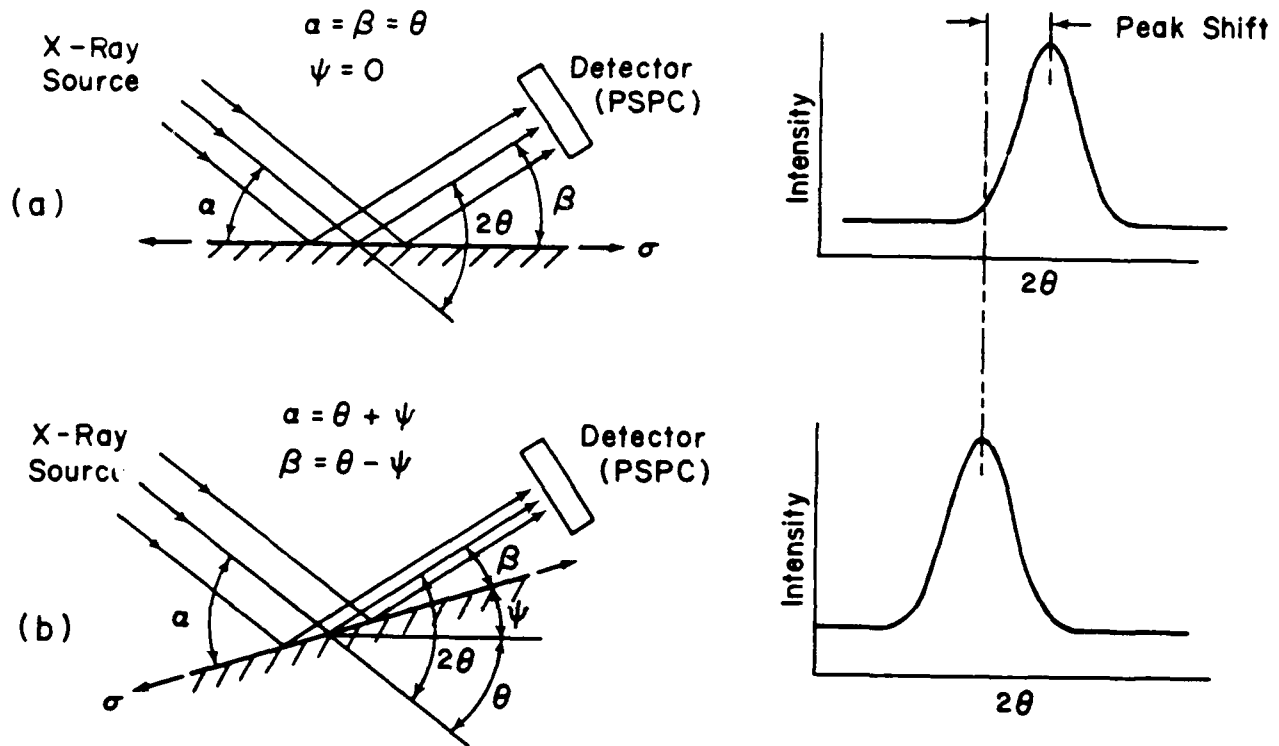
Figure 1. Residual stress measurement by X-ray diffraction (adapted from TEC manual [9]).

where λ is the wavelength, n is the order of reflection, and d is the interplanar spacing. The diffraction angle 2θ, is the angle between the diffracted beam and the incident beam, and is measured experimentally. Figure 1 is a schematic illustration showing how x-ray diffraction occurs and also shows the effect of a change in ψ, where ψ is the angle between the diffraction vector (which is the bisector of the incident beam and the diffracted beam) and the normal to the sample. In the figure, α and β are the incident and diffracting angles respectively. If planes of atoms lying parallel to the surface [with an interplanar spacing "d"] satisfy Bragg's law, diffraction will occur as shown in Figure 1(a). This diffraction occurs from a thin surface layer of approximately $20\mu m$. When the specimen is tilted with respect to the incident beam by an angle ψ, a different set of grains diffract, and the orientation of the diffracting planes change. When a uniform stress is applied on the sample, as the planes that are diffracting are different, the value of d is changed. From Bragg's law, a change in the d-spacing leads to a corresponding change in 2θ. The presence of a surface stress in the sample is reflected as a shift in the diffraction peak on an Intensity - 2θ plot as shown in Figure 1. Strain in the sample is reflected as a change in the inter-planar spacing d_{hkl} of a set of diffracting planes (hkl). This variation Δd is measured from Bragg's law as

$$\varepsilon = \frac{\Delta d}{d_{hkl}} = -(\cot \theta)\, \Delta \theta \qquad (2.02a)$$

Solving for $\Delta \theta$ we have,

$$\Delta \theta = -\frac{\Delta d}{d_{hkl}}\,(\tan \theta) = -\varepsilon \tan \theta \qquad (2.02b)$$

where $\Delta \theta$ is the shift in the diffraction peak. From the value of the 2θ peak and Bragg's law, the spacing of the planes for the corresponding orientation can be obtained. From equation (2.02b), it is evident that, x-ray diffraction measurements at high angles have a greater resolution in θ. This is because for a given ε, as θ increases, $\tan\theta$ increases resulting in an increased sensitivity and therefore a greater resolution in θ.

The theoretical developments necessary for the treatment of lattice strains and their relation to
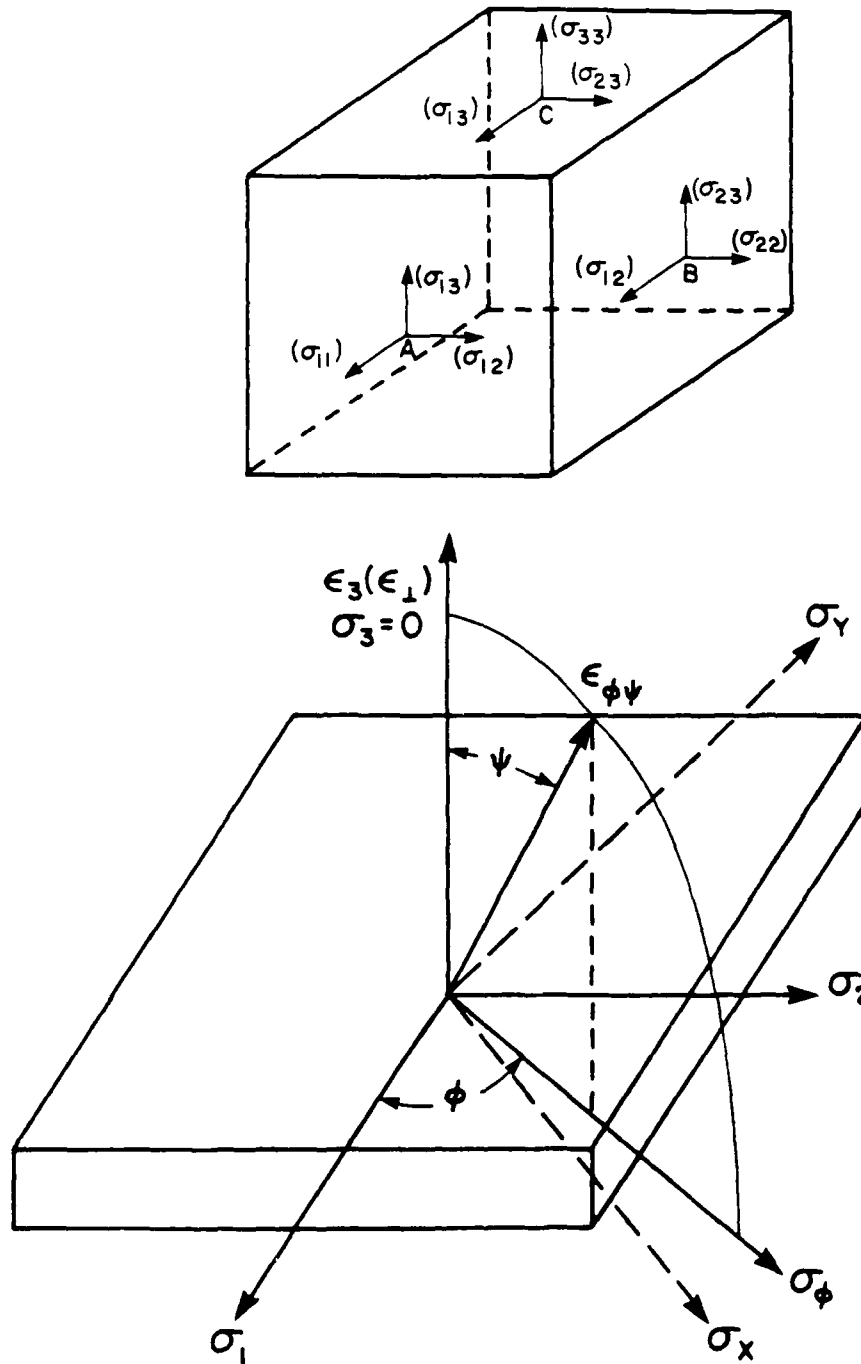
Figure 2.   (a) State of stress in a homogenous isotropic solid (Noyan
and Cohen [7]), (b) Stress in a biaxial system (Hilley, Ed [6]).

stresses follow from the classical theory of elasticity. The state of stress on any element in a homogeneous isotropic solid (Figure 2a), is described by three normal components σ_{11}, σ_{22}, σ_{33} and six shear components σ_{12}, σ_{13}, σ_{23}, σ_{21}, σ_{31}, and σ_{32}. The stress tensor σ_{ij} (i = 1,2,3; j = 1,2,3) has been proved [5] to be a second rank symmetric tensor. This implies that $\sigma_{ij} = \sigma_{ji}$, and the number of independent shear stresses is reduced to three.

The relation of the strain equation obtained from the classical theory of elasticity to x-ray stress analysis has been presented by Hilley [6]. Figure 2b illustrates a flat metal surface wherein σ_{11}, σ_{22}, σ_{33} and ε_{11}, ε_{22}, ε_{33} are the principal stresses and strains respectively. For any stress component σ_{ij}, from elasticity theory, the strain in any direction making angles ϕ and ψ with σ_{11} and σ_{33} respectively is given by

$$\varepsilon_{\phi\psi} = \frac{d_{\phi,\psi} - d_o}{d_o} = \frac{S_2}{2}\left[(\sigma_{11}\cos^2\phi + \sigma_{12}\sin^2\phi + \sigma_{22}\sin^2\phi - \sigma_{33})\sin^2\psi - \sigma_{33}\right]$$

$$+ S_1(\sigma_{11} + \sigma_{22} + \sigma_{33}) + \frac{S_2}{2}(\sigma_{13}\cos\phi + \sigma_{23}\sin\phi)\,sin2\psi \qquad (2.03)$$

If the x-ray diffraction measurements are confined to the surface, then plane stress conditions are assumed to exist. In the event of plane stress conditions and the absence of shear stresses, equation (2.03) reduces to

$$\varepsilon_{\phi\psi} = \frac{d_{\phi,\psi} - d_o}{d_o} = \frac{S_2}{2}(\sigma_{11}\cos^2\phi + \sigma_{22}\sin^2\phi)\sin^2\psi - S_1(\sigma_{11} + \sigma_{22}) \qquad (2.04)$$

In this equation, $d_{\phi,\psi}$ is the spacing of the planes whose normal makes angles ϕ and ψ with σ_{11} and σ_{33} respectively. $S_2/2$ and S_1 are the elastic constants. For an isotropic medium,

$$S_2/2 = (1 + v)/E \qquad \text{and} \qquad S_1 = -v/E,$$

where E is the Young's modulus and v is Poisson's ratio. When $\psi = 90°$, the surface stress component σ_ϕ is given by

$$\sigma_\phi = \sigma_1\cos^2\phi + \sigma_2\sin^2\phi \qquad (2.05)$$

Substituting equation (2.05) into equation (2.03), we have,

$$\varepsilon_{\phi\psi} = \frac{d_{\phi,\psi} - d_o}{d_o} = \frac{S_2}{2}\sigma_\phi \sin^2\psi - S_1(\sigma_1 + \sigma_2) \tag{2.06}$$

When ψ is zero, the x-ray beam detects the strain in the z i.e. the ε_{33} direction. This strain is given by,

$$\varepsilon_{\phi,o} = \varepsilon_{33} = \frac{d_{\phi,o} - d_o}{d_o} \tag{2.07}$$

Here $d_{\phi,o}$ is the spacing of the planes reflecting under stress at $\psi = 0$. The strain ε_{33} has a finite value, given by the Poisson contractions due to σ_{11} and σ_{22} as

$$\varepsilon_{33} = - S_1(\sigma_{11} + \sigma_{22}) \tag{2.08}$$

Subtraction of equation (2.08) from equation (2.06) yields

$$\varepsilon_{\phi,\psi} - \varepsilon_{33} = \frac{S_2}{2}\sigma_\phi \sin^2\phi \tag{2.09}$$

This is the basic equation which relates the lattice strains to stresses, and is utilized in the x-ray diffraction method of stress measurement. This equation is for conditions of plane stress. Expressing the strains in terms of plane spacings, we have

$$\frac{d_{\phi,\psi} - d_o}{d_o} - \frac{d_{\phi,o} - d_o}{d_o} = \frac{d_{\phi,\psi} - d_{\phi,o}}{d_o} = \frac{\sigma_\phi}{E}(1 + v)\sin^2\psi \tag{2.10}$$

Equation (2.10) predicts a linear variation of d vs $\sin^2\psi$. The surface stress σ_ϕ in any direction on the surface of the specimen can be obtained from the slope of a least-square line fitted to the experimental data, measured at different ψ. As multiple ψ-tilts are utilized, this procedure is known as the $\sin^2\psi$ technique. As $d_{\phi,\psi}$, $d_{\phi,o}$ and d_o are very nearly equal to one another, $(d_{\phi,\psi} - d_{\phi,o})$ is small compared to d_o. The unknown spacing d_o can therefore be replaced in the denominator of equation (2.10) by $d_{\phi,\psi}$ or $d_{\phi,o}$. For most materials, it has been reported by Noyan and Cohen [7] that the

error introduced by the elastic strain due to the above substitution is small and is of the order of 0.1 %. Equation (2.10) can now be written as

$$\sigma_\phi = \frac{E}{(1 + v) \sin^2\psi} \ \frac{d_{\phi,\psi} - d_{\phi,o}}{d_{\phi,o}} \qquad (2.11)$$

The elastic stress constants $S_2/2$ and S_1 are known to vary with the crystallographic directitions in an anisotropic material. As the strains are measured in particular crystallographic directions, the mechanically measured values of these constants cannot be directly applied for diffraction measurements. It is hence imperative to experimentally determine the elastic constants in the measurement of stress by x-ray diffraction. The Four-Point Bend Method has been found by Prevey [8] to be a standard and a simple method for experimentally determining this x-ray elastic constant parameter. It is also possible to calculate them from single crystal elastic constants. A list of values of the elastic constants has been compiled by Technology for Energy Corporation [9] and by James listed in the book by Noyan and Cohen [7].

The manual measurement of residual stress requires the accumulation of x-ray counts, for different ψ angles with the first ψ angle being equal to zero. The accumulation times for these are long. If the intensities are collected using a hardware controlled step scan, the operator time arising from long collection times can be saved. Thus, with a system that includes hardware and software for on-line computer control [10], the operator is just required to set the sample in the diffractometer and start the program. All essential procedures like peak location, selection of three angles, collection of x-ray counts, correction of intensities, calculation of peak angles and stress, and report of the data, are controlled by the computer.

The last decade has seen an increase in the instrumentation of x-ray diffraction, offering automation in the measurement of stresses using x-rays. Instrumentation such as Fastress [11] and systems sold by Rigaku-Denki of Japan offer automation nonetheless, but at the expense of precision and versatility. Neither method measures a full diffraction peak. Hence, corrections for secondary effects like Lorentz polarisation, sample absorption, beam geometry, resolution of the K_a doublet arising

13

out of anisotropic cold work, etc., cannot be made. The computer automated stress analysis system reported by Koves and Ho [12] lack on-line control for locating peaks, which requires the collection of many data points and off-line calculation of residual stresses.

The use of position sensitive detectors makes it possible to record an entire diffraction peak without moving the diffractometer. Position sensitive proportional counters [13] not only process the presence of a photon, but also its location along a line, so that data can be recorded simultaneously from a range of 2θ angles. This results in a considerable reduction of data acquisition time. Also, the absence of the motion of the detector to record a peak eliminates the heavy and expensive gearing characteristics of a conventional diffractometer. A portable x-ray stress analyzer based on one such position sensitive detector was used by James and Cohen [14] for residual stress measurements.

Various methods of x-ray diffraction have been used for residual stress measurements for different applications. However, measurements have yet to be made on test specimens mounted in a testing machine. Measurement time is crucial in applications which require the study of time dependent relaxation of residual stresses. Such measurements cannot be made using a traditional x-ray system due to excessive measurement times. Moreover, the heavy gearing characteristics of such a system creates a problem in the portability of the equipment to the test site.

The state-of-the-art x-ray stress analysis system manufactured by Technology for Energy Corporation, Knoxville, TN, is being used for making such measurements on notched tensile specimens. This system is based on the work of James and Cohen [15-18]. The system consists of newly designed portable diffractometer, a position-sensitive proportional counter, signal-processing electronic system, an x-ray source and power supply, a collimator and shutter, an articulated arm diffractometer support, a DEC LSI-11/23 Plus microcomputer with dual floppy disk drives, a printer-plotter, a graphics display terminal, and an x-ray safety system [9]. All components are mounted in an air-conditioned mobile cart. An entire set of software is available for data acquisition, calibration and data analysis.

14

A distinct advantage of the advanced x-ray system is that it is highly compact and portable. The instrumentation can be mounted for work on a specimen in a mechanical testing machine and can remain in position for measurements during brief pauses in a fatigue test. This avoids lost data due to the delay that would otherwise be involved in removing the test specimen for study. It also lessens the chance of accidental damage or compromised specimen alignment, both of which are more likely if test specimens must be repeatedly removed and remounted in the testing machine. A brief description of the experimental set-up used for making measurements along the edge of a notched tensile specimen, at the bottom of the notch, is given by Dowling and Ranganathan [19].

THIS PAGE INTENTIONALLY LEFT BLANK

3.0 Stress Distribution Model

3.1 Introduction

When a polycrystalline metal undergoes deformation with the strain being uniform over large distances relative to the grain size, the elastic portion of the strain causes the interplanar spacings to change from their standard stress free value. The change is dependent on the magnitude of the applied stress. This change is indicated by a shift in the diffraction lines as a function of 2θ positions. The shift in the Bragg angle position (2θ) due to the strain can be determined experimentally from which the elastic strain can be calculated. Once the elastic strain is known, the stress can be calculated by a calibration procedure, or from stress-strain relations.

In the analytical work done in the present work, the stress state in a notched specimen subjected to uniaxial loading was first simulated, which is presented in this section.

17

A material is designated as elastic if it obeys Hooke's law of elasticity. In this limit, the ratio of the maximum stress to the nominal stress is termed as the stress concentration factor. This factor is known to be dependent on the type of loading and the geometry of the specimen. The presence of a notch leads to a stress variation in the immediate vicinity of the notch. At large distances away from the notch, the stress distribution is not affected by the notch; for example, it is uniform for simple axial loading. The shape of the notch in a notched specimen is of critical importance in assessing the stress gradients present in the vicinity of the notch. The curvature at the base of the notch is of greater importance than the flank angle. In the case of a double edged notch specimen as shown in Figure 3, the ratio of half the distance between the notches "a", and the radius of curvature at the notch tip ρ, is a non-dimensional ratio termed as the "notch curvature". The stress concentration factor has been found to depend on this ratio [20]. In a specimen with a shallow notch, the stress concentration factor is independent of the width of the specimen. In a specimen with a deep notch, the stress concentration factor is a function of the notch curvature alone, the effect of the depth of the notch being insignificant as the stresses fall off rapidly as we go farther away from the notch. As a limiting condition, when h, the depth of the notch, is zero, the stress concentration factor becomes equal to unity .

A double edged notch specimen with a flank angle of 30° from the center line was used for this investigation. The notches have a root radius of ρ. On the plane surface, the notch tips are separated by a distance 2a. A schematic illustration of the specimen geometry is shown in Figure 3. Machine drawings of the specimen are shown in Figure 4.

3.2   Stress distribution calculations

The most commonly used coordinate system for stress and strain calculations is the Cartesian coordinate system. An important criterion for the calculation of the stresses acting on the surface of

2a = 0.50"

ρ = 0.125"

t = 0.342"

p = 70.0ksi

p

t

Y

Z

2a

ρ

X

surface A

surface B

w
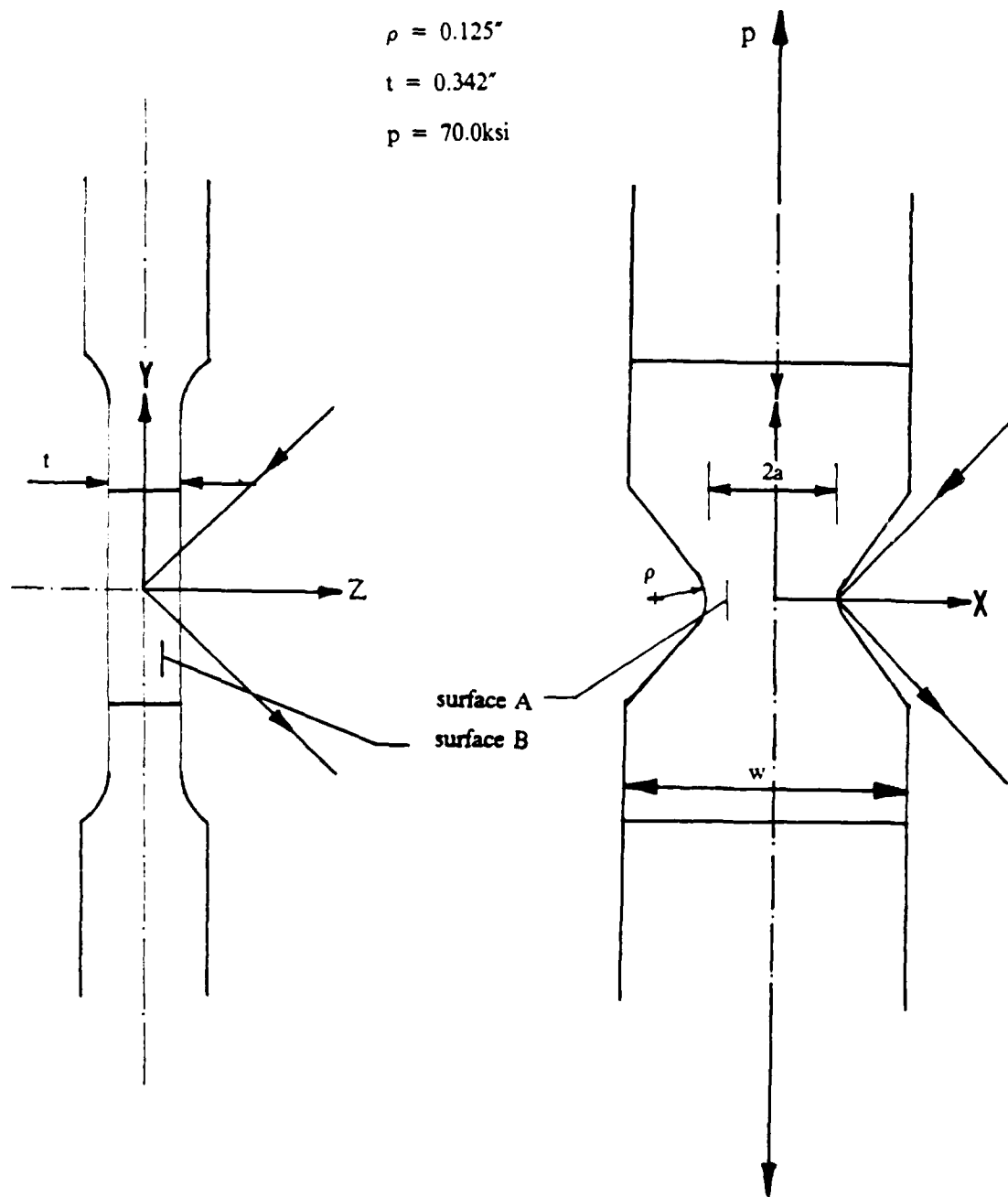
Figure 3. A schematic of the specimen geometry.
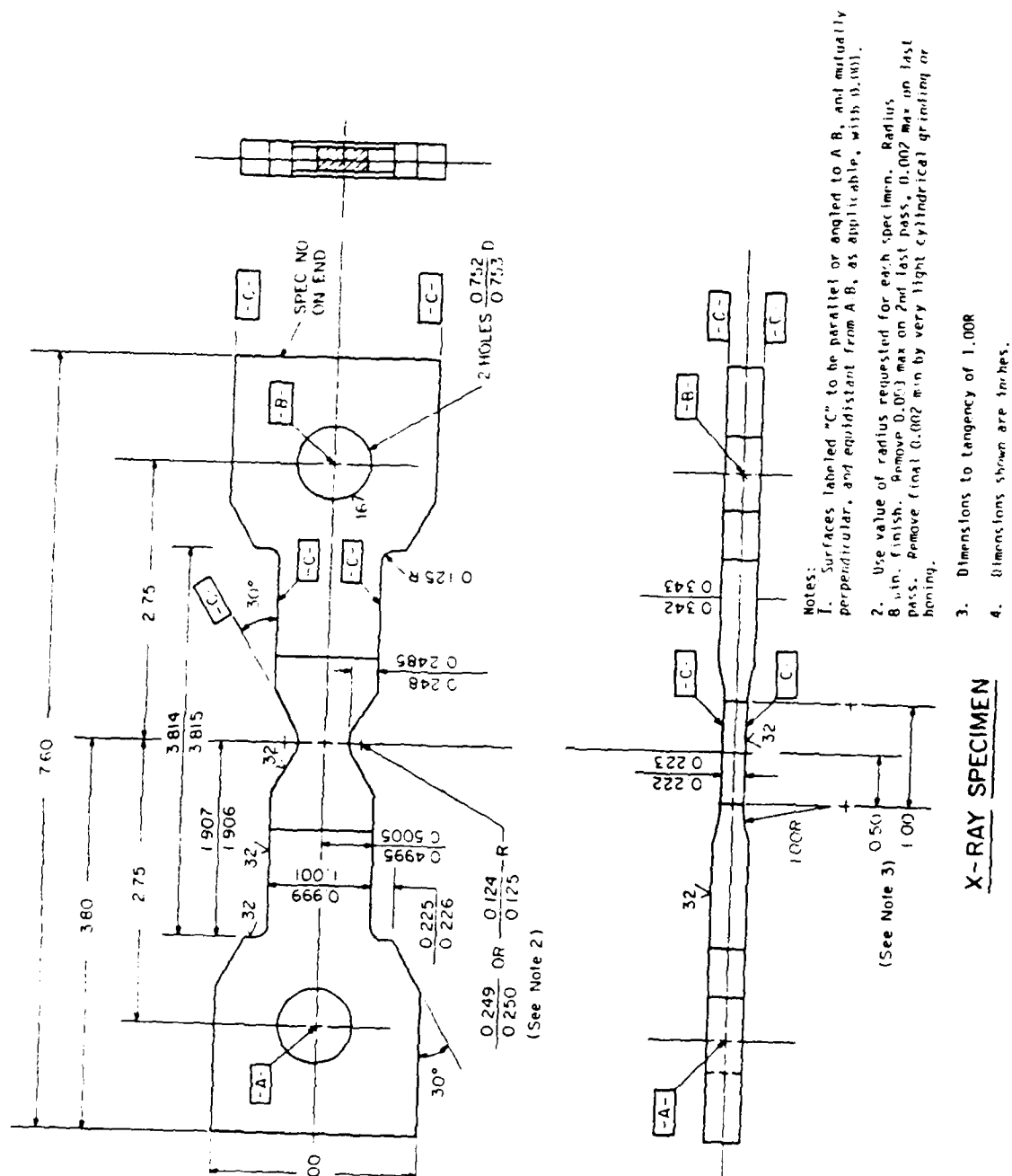
Figure 4.   Machine drawings of the specimen.

20

a body is the satisfaction of the boundary conditions. In most cases, as the body is curved, it is difficult to satisfy the conditions using the Cartesian system. It is hence preferable to use a curvilinear system of coordinates for such calculations.

The three orthogonal directions in the curvilinear system of coordinates are u, v and w. These and the cartesian coordinates x, y and z are assumed to be differentiable and are related by the following relations:

$$x = x(u,v,w), \quad y = y(u,v,w) \quad and \quad z = z(u,v,w) \qquad (3.01)$$

In the curvilinear system of coordinates, the surfaces are defined by u = constant, v = constant and w = constant. The direction of u at any point is given by the normal to the surface u = constant. Thus, in an area where u is constant, the distance between two adjacent surfaces separated by a differential du is given by $h_u du$, where h_u is termed as the factor of distortion to account for the curvilinear distortion resulting from differing curvature of the two surfaces. The factors of distortion for the surfaces where v and w are constant, are given by, h_v and h_w respectively.

The direction cosines between the two co-ordinate systems are given by the cosine of the angle between the linear element h_u and it's corresponding component as shown in Figure 5. The angles between the u direction in the curvilinear system and the x direction in the cartesian system is given by

$$\cos(x,u) = \frac{1}{h_u} \frac{\partial x}{\partial u} \qquad (3.02)$$

The corresponding angles of u with y and z and those of v and w with x, y and z can be calculated by similar equations.

Considering a biaxial system such as a bar with deep hyperbolic notches, the curvilinear coordinates u and v can be related to the cartesian coordinates by the relations
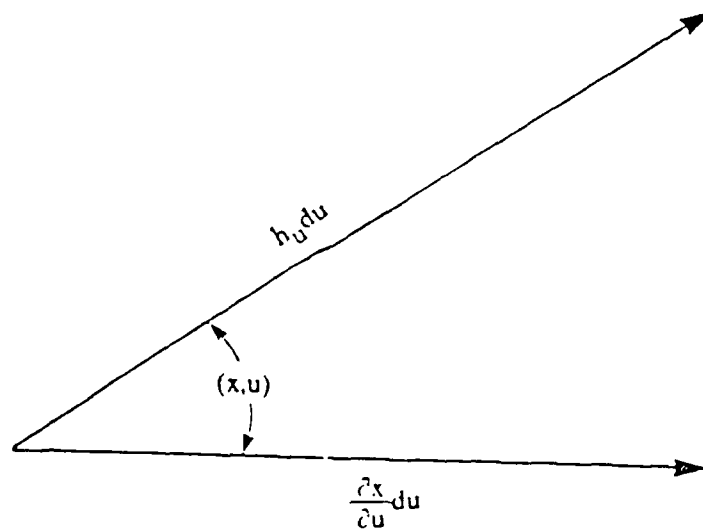
Figure 5. Direction cosine between the two coordinate systems.

$$x = c \cosh u \sin v$$
$$y = d \sinh u \cos v$$

(3.03)

Thus the lines $u = constant$ are ellipses and the lines $v = constant$ are hyperbolas; c and d are normalizing factors between the two coordinate systems.

Neuber [20], has derived the stresses in cylindrical coordinates for a bar with infinitely deep hyperbolic notches, in uniaxial tension. The normal stresses in the u and v directions and the shear stress are given by the following equations.

$$\sigma_u = \frac{A}{h^4} \cosh u \cos v \, (2h^2 + \cos^2 v_o - \cos^2 v)$$

$$\sigma_v = \frac{A}{h^4} \cosh u \cos v \, (\cos^2 v - \cos^2 v_o)$$

(3.04)

$$\tau_{uv} = \frac{A}{h^4} \sinh u \sin v \, (\cos^2 v_o - \cos^2 v)$$

where h is the factor of distortion and is found from the Jacobian of the two systems and is given by

$$h_u^2 = h_v^2 = h_w^2 = h^2 = \sinh^2 u + \cos^2 v,$$

(3.05)

A is a dimensionless constant given in terms of the nominal stress p (the mean stress over the narrowest cross-section under tensile loading) as,

$$A = p \, \frac{\sin v_o}{v_o + \sin v_o \cos v_o},$$

(3.06)

and v_o is the hyperbola parameter. A definite notch contour corresponds to every value of v_o and this is related to the notch curvature $(\frac{a}{\rho})$ by

$$\tan^2 v_o = \frac{a}{\rho}$$

(3.07)

23

Using the two relations for the coordinate transformation, we have, for a point on the hyperbola (and hence $v = v_o$),

$$u = \sinh^{-1}\left[\frac{(y/d)}{\cos v_o}\right] \tag{3.08}$$

The maximum value of x, for each value of y/d is

$$x_{max} = c \cosh u \sin v$$

$$(x)_{y/d=0} = c \sin v_o = a$$

Hence,

$$x_{max} = a \cosh u \tag{3.09}$$

In order to express the parameter v as a function of x and y, the coordinate transformation relations are used. The equation of the hyperbola is given by,

$$\frac{(x/c)^2}{\sin^2 v} - \frac{(y/d)^2}{\cos^2 v} = 1 \tag{3.10}$$

Solving this equation for v, we have,

$$\sin v = \left[\frac{\left[1 + (x/c)^2 + (y/d)^2\right] - \sqrt{\left[1 + (x/c)^2 + (y/d)^2\right]^2 - 4(x/c)^2}}{2}\right]^{-1/2} \tag{3.11}$$

Note that the positive value of the inner square root yields a value of $\sin v$ greater than 1 and hence has to be eliminated. Thus, summarizing the conditions for u and v, we have,

$$u = \sinh^{-1}\left[\frac{(y/d)}{\cos v_o}\right] \tag{3.12}$$

$$v = \sin^{-1}\left[\frac{\left[1 + (x/c)^2 + (y/d)^2\right] - \sqrt{\left[1 + (x/c)^2 + (y/d)^2\right]^2 - 4(x/c)^2}}{2}\right]^{-1/2} \tag{3.13}$$

24

The values of the stresses in curvilinear coordinates can be calculated for any point in the x-y plane, in the region between the notches.

By simple coordinate transformation, the corresponding Cartesian components are found to be

$$\sigma_x = \left(\frac{\sigma_u + \sigma_v}{2} \right) + \left(\frac{\sigma_u - \sigma_v}{2} \right) cos\, 2\alpha - \tau_{uv} sin\, 2\alpha$$

$$\sigma_y = \left(\frac{\sigma_u + \sigma_v}{2} \right) - \left(\frac{\sigma_u - \sigma_v}{2} \right) Cos\, 2\alpha + \tau_{uv} sin\, 2\alpha \qquad (3.14)$$

$$\tau_{xy} = \left(\frac{\sigma_u - \sigma_v}{2} \right) sin\, 2\alpha + \tau_{uv} cos\, 2\alpha$$

where α is the angle between the tangent to the curve v = constant, in the direction u increasing, and the x-axis, and is given by

$$cos\, \alpha = \frac{1}{h} \frac{\partial x}{\partial u}$$

$$= \frac{c}{h}\, sinh\, u\, sin\, v \qquad (3.15)$$

Hence,

$$\alpha = cos^{-1} \left[\frac{c}{h}\, sinh\, u\, sin\, v \right] \qquad (3.16)$$

Thus, the equations presented here can be used to calculate the distribution of the stresses in the x and y direction as a function of the distance from the notch center line.

3.3 Results and discussion

The stress distribution presented thus far is for a specimen with deep hyperbolic notches in an infinitely wide plate. However, in order to extend these calculations for the notch specimen with a geometry as shown in Figure 3 , the following approximations have to be valid.

- Extension of the calculations for a specimen with infinite geometry to a specimen with finite geometry.

- Approximation of a notch with flank angles, to a hyperbolic notch.

Justifications for the above two approximations follow.

The stress concentration factors for two different notch curvatures are shown in Table 1. The values listed are for the cases of a specimen with finite and infinite width respectively. These values have been established from the Handbook of Stress Concentration Factors [21]. The stress concentration factor K_t was first obtained for a flat tension bar with opposite U-shaped notches for the a/ρ and w/a which is pertinent to our specimen geometry, where w is the width of the specimen. The stress concentration factor $K_{t\alpha}$ for the corresponding V-shaped notch with the flank angle α, was then estimated from a plot of $K_{t\alpha}$ vs K_t for different flank angles α, obtained from the same handbook. As is evident from the tabulated values, the error involved in extending the calculations from an infinite model to one of finite width is approximately 3 percent.

Kikukawa [22] conducted tests on a photoelastic model made with U-shaped notches having a/ρ = 3.0 and h/ρ ranging from 10.0 to 0.25. He reported that the largest increase in the stress concentration factor for notches of finite depth as compared to infinitely deep notches was 7 percent.

Table 1. Stress concentration factors for finite and an infinite model.

K_t	a/ρ = 2.0	a/ρ = 1.0
Infinite Model	1.96	1.55
Finite Model	2.02	1.61
Percentage Error	3.0	3.7
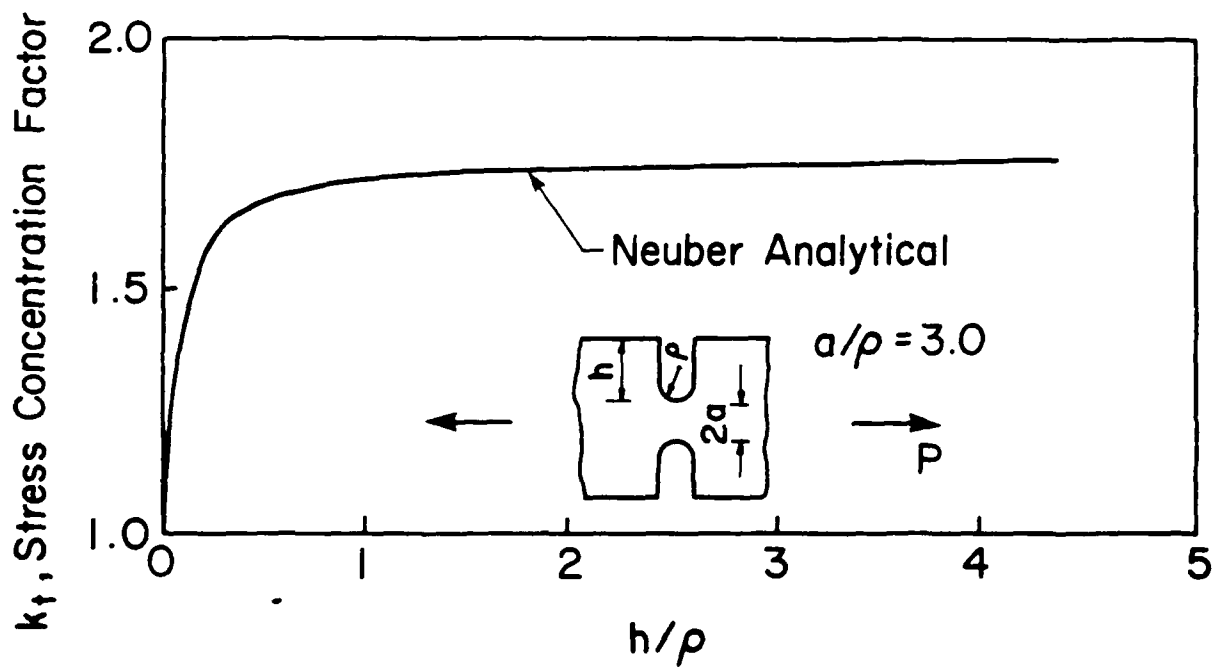
Figure 6. Neuber's estimate of stress-concentration factors for a tensile bar with U-shaped notches (Flynn & Roll [24]).

Neuber [20] made an analytical estimate of the stress concentration factor for a specimen with symmetric U-shaped notches having $a/\rho = 3.0$ and h/ρ ranging from 0 to 4.0. Figure 6 shows this estimate of the stress concentration factor. From the figure, it can be seen that the change in the stress concentration factor between $h/\rho = 1.0$ and 2.0 is approximately 8 percent. A point worth noting in this regard is that the stress concentration factor obtained by Kikukawa [23] for infinitely deep U-shaped notches was the same as the value obtained for infinitely deep hyperbolic notches. In all cases, Kikukawa [23], as reported by Flynn and Roll [24], found that for certain a/ρ ratios, the maximum stress concentration factor occurs with notches of finite depth rather than with infinitely deep notches. The difference in the stress concentration factors for the two cases is not significant. The stress distribution in the region between the notches is dependent on the stress concentration factor, with the maximum values of the stress being in the vicinity of the notches. As the difference in the stress concentration factors for the two models is not significant, the stress distributions for the two models are similar. Hence, extension of the calculation for a specimen with infinite geometry to a specimen with finite geometry is a valid approximation.

The stress distribution obtained for σ_x and σ_y from equation (3.14) the calculations are plotted as a function of the distance from the centerline in Figure 7. This stress variation is for the surface A of the specimen. Figure 7 illustrates the variation of both the x and y component of the stress ie., σ_x and σ_y, in the region between the notches on surface A of the specimen. The co-ordinate axis is as shown in Figure 3, with the origin being at the centerline on surface A , in the region between the notches. The stresses were plotted for various heights (in inches), above the x-axis ie., for four different values of y.

The variation in σ_y is of importance from the point of view of the slit geometry being used in the experimental x-ray measurements. A 0.5mm by 5mm (0.02" by 0.2") rectangular slit is one of the slit geometries used in the experiments being conducted at Virginia Tech on the TEC x-ray system by other investigators. A cross-section of this slit is shown in Figure 7. The 5mm dimension in the longitudinal direction corresponds to 0.1 inches above the centerline. The variation in the peak
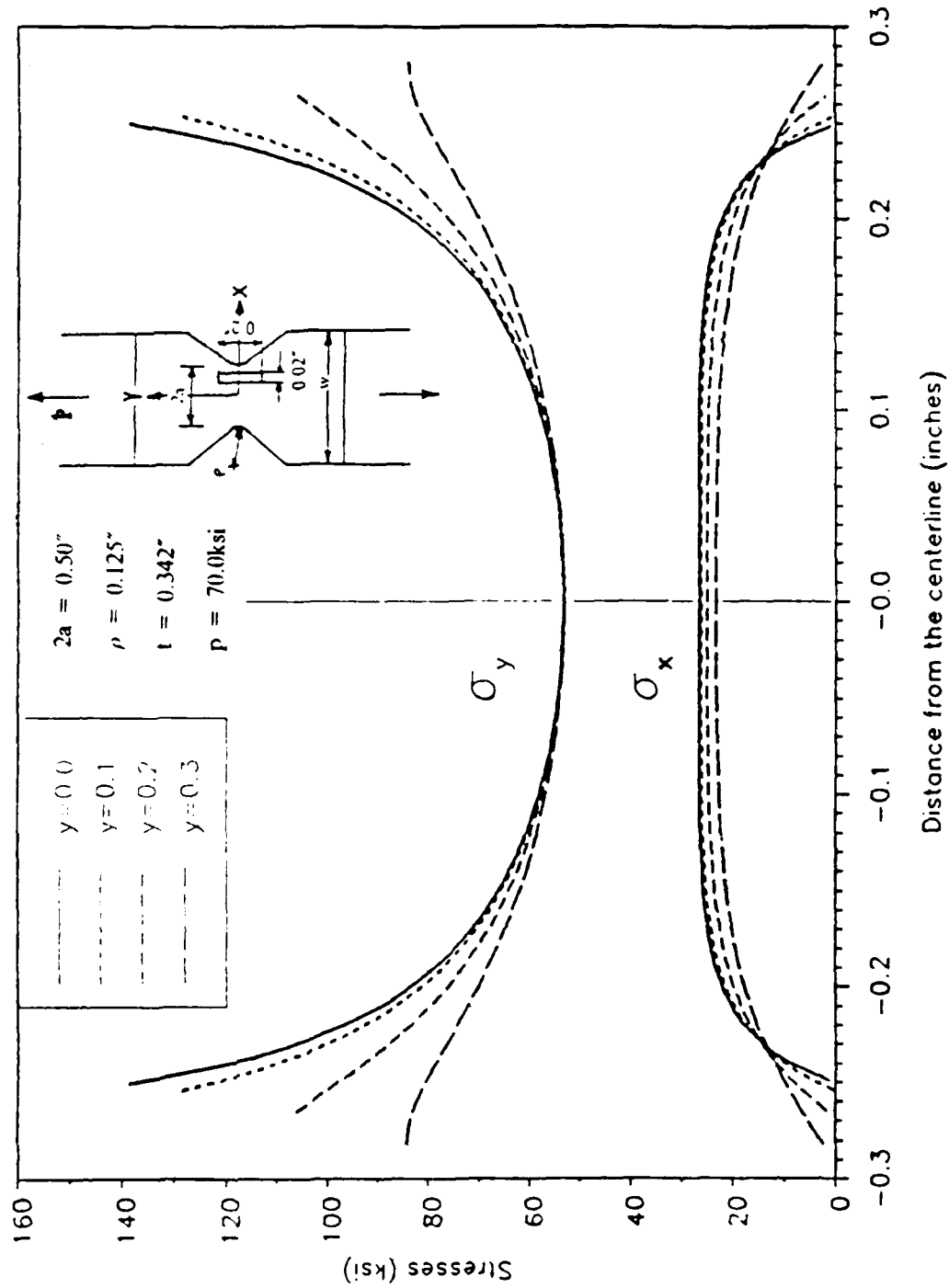
Figure 7.   Stress distribution in the region between the notches for different heights above the centerline.

stress corresponding to y = 0.0 and y = 0.1 is approximately 5%. At regions farther away from the notch, this variation is seen to be negligible. This implies that the above orientation of the slit is good for the x-ray measurements. Also, the negligible variation in the stress up to a certain height above the x-axis helps in justifying the approximation of a V-notch with a flank angle to a hyperbolic notch. This approximation is however not valid beyond a certain height above the notch centerline, due to the considerable change in the peak stress as seen in the dotted curves of Figure 7. Any misalignment in the slit orientation along the y axis would cause detection of the variation in the peak stress corresponding to y greater than 0.1.

The stress distribution obtained so far is used as the basis for the x-ray diffraction model dealt with in the next section.

3.4 Calculation of strains

As strain is the quantity which is measured experimentally, it is important to establish relations for strains in the three orthogonal directions. This is done using Hooke's law of elasticity. The corresponding elastic strains are obtained from the following equations. In a plane stress condition, $\sigma_z = 0$.

$$\epsilon_x = \frac{1}{E}(\sigma_x - \nu\sigma_y)$$
$$\epsilon_y = \frac{1}{E}(\sigma_y - \nu\sigma_x) \qquad (3.17)$$
$$\epsilon_z = -\frac{\nu}{E}(\sigma_x + \sigma_y)$$

where ν and E are the Poisson's ratio and the Young's modulus respectively. Values for ν and E for 7475 Al were obtained from the book by Byars and Snyder [25] and are given in Table 2. Note that, although $\sigma_z = 0$, there is a strain in the z direction (ϵ_z) due to Poisson effect.
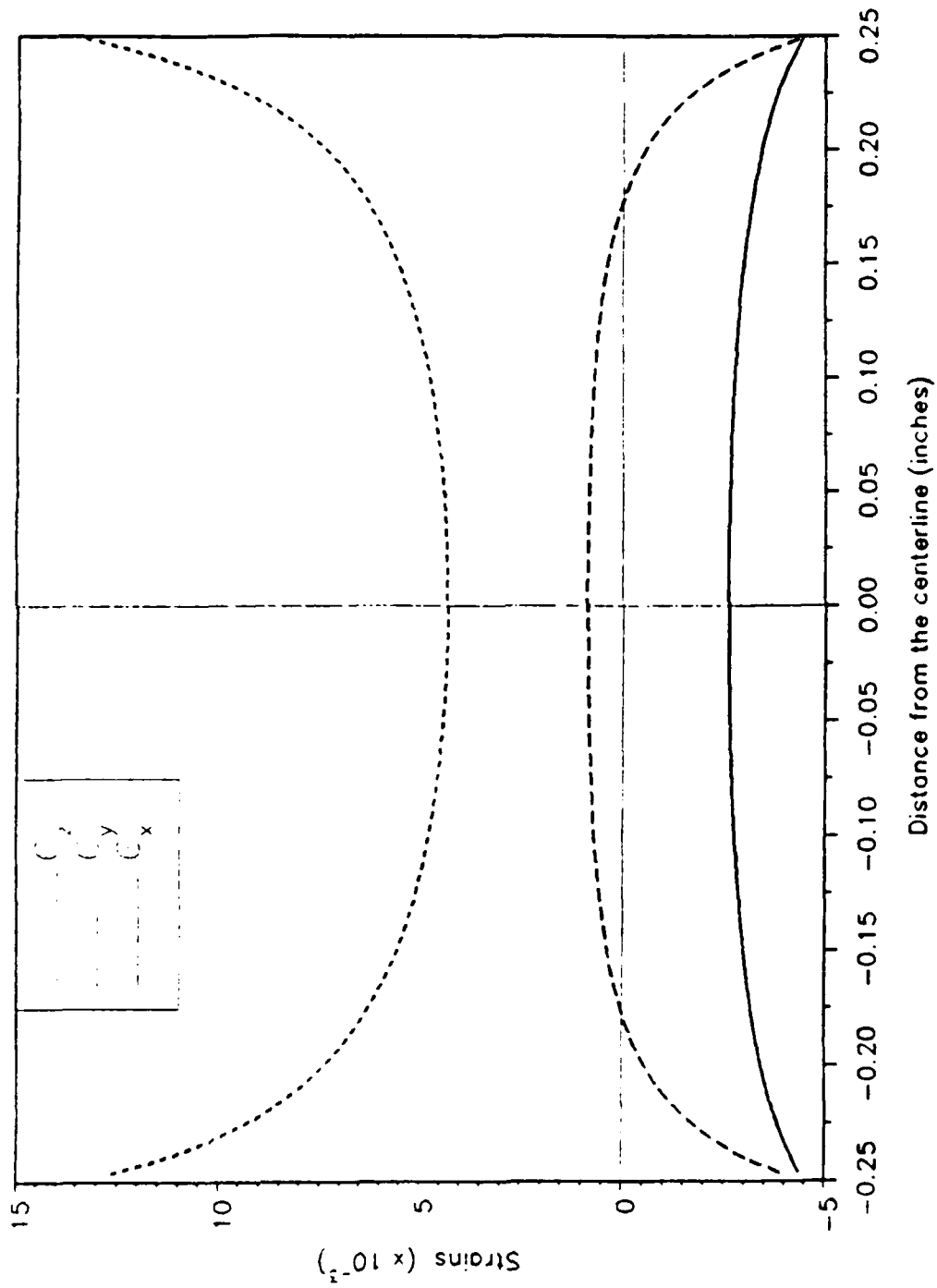
Figure 8.   Strains distribution in the region between the notches as a function of distance from the centerline.

The plot of the strains as a function of the distance from the centerline is shown in Figure 8. The strains in the x and z directions are compressive due to Poisson contraction. The strains thus obtained were used in determining the d-spacing profile from which the intensity profiles were simulated.

THIS PAGE INTENTIONALLY LEFT BLANK

4.0 X-ray Diffraction Model

The d-spacing profiles, calculated from the strain distribution described in the previous chapter, are presented in this section. An analytical model which simulates the state of stress developed during experiments conducted on notched tensile specimens is described. The x-ray response from this model was obtained in order to control, study and interpret the x-ray effects that are seen during testing. The presence of a stress in the specimen is indicated by changes in the d-spacings of the diffracting planes. The line profiles resulting from the d-spacing variation on the flat surface (Λ) of the specimens were simulated. These profiles were obtained, as x-ray effects from individual grains, for a beam of finite size. They arise as a result of a strain gradient present at the specimen surface. The effects of the depth of penetration of the x-ray beam on the stress gradient occuring on surface B (edge) of the specimen is also discussed in this section. Sample calculations for a 7475 Al notched tensile specimen are also presented.

4.1 Model for residual stress measurement

The strains obtained from the stress distribution model were used to calculate the variation in the inter-planar spacings. From the x-ray definition of strain, it is known that the shift of the diffraction lines to new 2θ positions, i.e., the difference in the d-spacings for the stressed and the unstressed state is related to the uniform macro-strain that causes the shift by the relation,

$$\varepsilon_{\phi,\psi} = \frac{d_{\phi,\psi} - d_o}{d_o} \tag{4.01}$$

where,

$\varepsilon_{\phi,\psi}$ is the strain in a direction making angles ϕ and ψ with σ_{11} and σ_{33} directions (Figure 2),

$d_{\phi,\psi}$ is the spacing under stress of the planes normal to the direction making angles ϕ and ψ with σ_{11} and σ_{33} respectively, and

d_o is the spacing of the same planes in the absence of stress.

When $\psi = 0$, the x-ray beam detects the strain in the z direction. This strain is given by

$$\varepsilon_{\phi,o} = \varepsilon_{33} = \frac{d_{\phi,o} - d_o}{d_o} \tag{4.02}$$

Here $d_{\phi,o}$ is the spacing of the planes reflecting under stress at $\psi = 0$. The relation for the difference between the two strains is given by equation (2.09) as,

$$\varepsilon_{\phi,\psi} - \varepsilon_{33} = \frac{\sigma_\phi}{E} (1 + v) \sin^2\psi \tag{4.03}$$

where σ_ϕ is the surface stress component. Again, from equation (2.10) we have,

$$\frac{d_{\phi,\psi} - d_o}{d_o} - \frac{d_{\phi,o} - d_o}{d_o} = \frac{d_{\phi,\psi} - d_{\phi,o}}{d_o} = \frac{\sigma_\phi}{E} (1 + v) \sin^2\psi \tag{4.04}$$

The above equation is based on the following assumptions.

- The material is isotropic and homogeneous in all of the volume irradiated by x-rays.

- Since measurements are confined to a small depth below the surface, plane stress conditions are assumed to exist.

- Shear stresses are absent in the irradiated volume.

The stress σ_ϕ can be obtained from the slope of a least-squares line fitted to experimental data measured at various ψ if the constants E, and v are known. The lattice spacing of the planes in the unstressed state, d_o, may not be available in practice. The lattice spacing measured at $\psi = 0$ is substituted for d_o. It has been reported by Noyan and Cohen [7] that for an elastic strain, the error introduced due to this substitution is only 0.1 percent. Equation (4.04) can now be written as

$$\sigma_\phi = \frac{E}{(1 + v)\sin^2\psi} \ \frac{d_{\phi,\psi} - d_{\phi,o}}{d_{\phi,o}} \qquad (4.05)$$

For the purpose of this simulation, the value of d_o was used as a scaling factor in the calculation of the d-spacing profile. The values of d_o for reflections from the (200), (400) and (333) planes were obtained from Pearson's Handbook [26]. These values and the wavelength of the radiation used are listed in Table 2. Table 2 also contains the values of the Young's modulus E and Poisson's ratio v used in the calculations. All the parameters are listed for a 7475 Al notched tensile specimen.

The fundamental equations in the x-ray diffraction measurement of stresses are now used to develop a model for the determination of residual stresses on the flat face, surface A (Figure 3) of the specimen in the region between the notches and, on the edge, surface B of the specimen at the bottom of the notch (notch tip). This model will be of help in the analysis of the stress state resulting from the experiments being conducted in the notched specimen. From equation (2.03), the strain in any direction can be determined. A coordinate system in which, the unprimed quantities refer to the specimen axis and the primed quantities imply laboratory coordinates is used, following the con-

Table 2. Material parameters.

Item	7475 Al
Radiation	Cu
λ (Å)	1.54178
Rectangular * Slit Size, mm	.5 by 5.0
d_0 (Å) (200) (400) (300)	2.0235 1.0117 0.7788
E (ksi)	10300
ν	0.33

* 5mm dimension parallel to specimen thickness.

vention established by Dolle [27]. The strain $\varepsilon_{33'}$ in the direction normal to the diffracting planes can be determined from

$$
\begin{aligned}
\varepsilon_{33'}(\phi,\psi) &\equiv \frac{d_{\phi,\psi} - d_o}{d_o} \\
&= \left[\varepsilon_{33} + (\varepsilon_{11}\cos^2\phi + \varepsilon_{12}\sin^2\phi + \varepsilon_{22}\sin^2\phi - \varepsilon_{33})\sin^2\psi + (\varepsilon_{13}\cos\phi + \varepsilon_{23}\sin\psi)\sin 2\psi\right]
\end{aligned}
\tag{4.06}
$$

Assuming the absence of shear strains, we have

$$
\varepsilon_{12} = \varepsilon_{13} = \varepsilon_{23} = 0
$$

Using this condition, equation (4.06) becomes

$$
\begin{aligned}
\varepsilon_{33'}(\phi,\psi) &\equiv \frac{d_{\phi,\psi} - d_o}{d_o} \\
&= \left[\varepsilon_{33} + (\varepsilon_{11}\cos^2\phi + \varepsilon_{22}\sin^2\phi - \varepsilon_{33})\sin^2\psi\right]
\end{aligned}
\tag{4.07}
$$

and hence $d_{\phi,\psi}$ can be expressed in terms of the strains by,

$$
\begin{aligned}
d_{\phi,\psi} &\equiv d_o(1 + \varepsilon_{33'}) \\
&= d_o\left[(1 + \varepsilon_{33}) + (\varepsilon_{11}\cos^2\phi + \varepsilon_{22}\sin^2\phi - \varepsilon_{33})\sin^2\psi\right]
\end{aligned}
\tag{4.08}
$$

Note that $\varepsilon'_{33}(\phi, 0) = \varepsilon_{33}$

The d-spacings at each point along the x-axis can be calculated from equation (4.08). Equation (4.08) relates to $d_{\phi,\psi}$ to principal strains. The strains calculated in the last chapter (Figure 8) were in the x, y, z system. The principal directions for cases A and B are different. In order to use equation (4.08) for both cases, two orthogonal coordinate systems were chosen in a principal strain space i.e., ε_{11}, ε_{22} and ε_{33} space which were then related to the strains ε_x, ε_y and ε_z. The values of the strains were obtained from the strain distribution in Figure 8. A figure of the specimen with the corresponding coordinate systems for surfaces A and B, is shown in Figure 9.

39

(b)   (a)
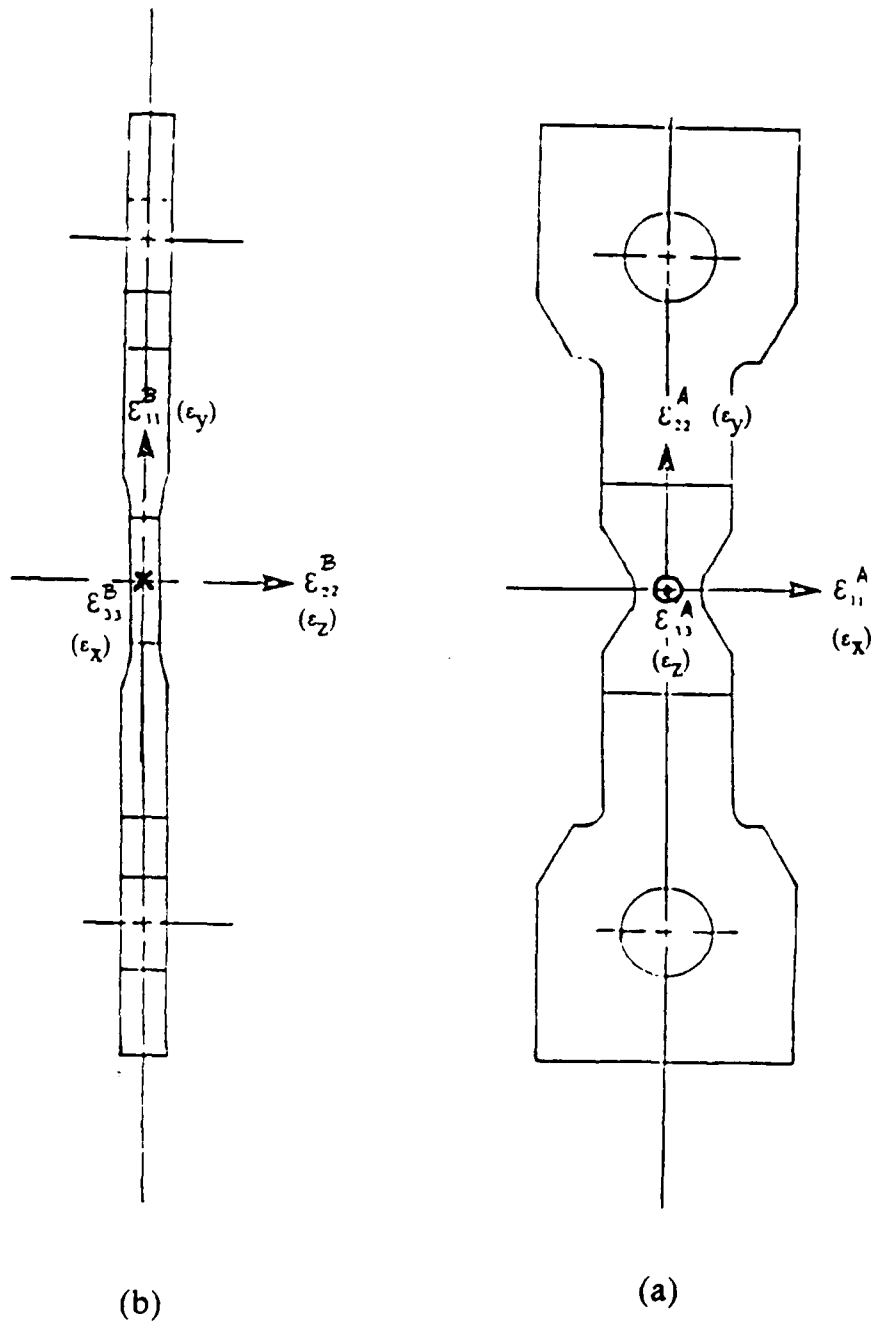
Figure 9.   A figure of the specimen showing the coordinate systems.

4.1.1   Plane surface (surface A)

With reference to the co-ordinate system in Figure 9(a), we have for measurements on surface A,

$$\varepsilon_{11} = \varepsilon_x$$

$$\varepsilon_{22} = \varepsilon_y$$

$$\varepsilon_{33} = \varepsilon_z$$

Substituting these into equation (4.07) we have,

$$\varepsilon_{33'}(\phi,\psi) \equiv \frac{d_{\phi,\psi} - d_c}{d_o}$$

$$= \left[\varepsilon_z + (\varepsilon_x \cos^2\phi + \varepsilon_y \sin^2\phi - \varepsilon_z) \sin^2\psi \right] \tag{4.09}$$

It is easy to verify that,

$$\phi = 0° \ , \ \psi = 0° \ , \ \varepsilon_{33'} = \varepsilon_z$$

$$\phi = 0° \ , \ \psi = 90° \ , \ \varepsilon_{33'} = \varepsilon_x \tag{4.10}$$

$$\phi = 90° \ , \ \psi = 90° \ , \ \varepsilon_{33'} = \varepsilon_y$$

as is required. The three different sets of values of ϕ and ψ correspond to three different positions of the x-ray source with respect to the specimen surface. These three positions correspond to the measurement of the d-spacings in each of the three orthogonal directions.

The d-spacing in any direction ϕ, ψ on surface A is obtained from equation (4.09) as,

$$\overset{A}{d_{\phi,\psi}} = d_o \left[(1 + \varepsilon_z) + (\varepsilon_x \cos^2\phi + \varepsilon_y \sin^2\phi - \varepsilon_z) \sin^2\psi \right] \tag{4.11}$$

This equation was used to calculate the d-spacing for $\phi = 0°$ and $90°$ at seven ψ values. These values are tabulated in columns II and IV of Table 3.

Table 3. d-spacing as a function of ψ at (-0.25, 0, 0)

$\sin^2 \psi$	$d^A_{0,\psi}$	$d^B_{0,\psi}$	$d^A_{90,\psi}$	$d^B_{90,\psi}$
0.00	0.77535	0.77535	0.77535	0.77535
0.07	0.77535	0.77628	0.77628	0.77535
0.25	0.77535	0.77885	0.77885	0.77535
0.50	0.77535	0.78234	0.78234	0.77535
0.75	0.77535	0.78584	0.78584	0.77535
0.93	0.77535	0.78840	0.78840	0.77535
1.00	0.77535	0.78934	0.78934	0.77535

4.1.2 Edge (surface B)

From the co-ordinate system shown in Figure 9(b), for measurements on surface B,

$$\varepsilon_{11} = \varepsilon_y$$

$$\varepsilon_{22} = \varepsilon_z$$

$$\varepsilon_{33} = \varepsilon_x$$

Consequently, equation (4.07) now becomes,

$$\varepsilon_{33'}(\phi,\psi) \equiv \frac{d_{\phi,\psi} - d_o}{d_o}$$

$$= \left[\varepsilon_x + (\varepsilon_y \cos^2\phi + \varepsilon_z \sin^2\phi - \varepsilon_x) \sin^2\psi \right]$$

(4.12)

It can again be verified for consistency that,

$$\phi = 0^\circ \ , \ \psi = 0^\circ \ , \ \varepsilon_{33'} = \varepsilon_x$$

$$\phi = 0^\circ \ , \ \psi = 90^\circ \ , \ \varepsilon_{33'} = \varepsilon_y$$

$$\phi = 90^\circ \ , \ \psi = 90^\circ \ , \ \varepsilon_{33'} = \varepsilon_z$$

(4.13)

Thus, the d-spacing in any direction ϕ, ψ on surface B can be obtained as,

$$\overset{B}{d_{\phi,\psi}} = d_o \left[(1 + \varepsilon_x) + (\varepsilon_y \cos^2\phi + \varepsilon_z \sin^2\phi - \varepsilon_x) \sin^2\psi \right]$$

(4.14)

This equation was used to calculate the d-spacing for $\phi = 0^\circ$ and 90° at seven ψ values. These values are tabulated in columns III and V of Table 3.

4.2   Discussion of the d vs sin² ψ results

The d-spacing values calculated from equations (4.11) and (4.14) are tabulated in Table 3. Equations (4.11) and (4.14) are dependent on the strains in the three orthogonal directions x, y and z. As the strain distribution (Figure 8) is a function of position along the x-axis, the d-spacing values can be calculated from equations (4.11) and (4.14) for various positions along the x-axis. The values listed in the table were calculated from the strain value at x = -0.25 (Figure 8). This corresponds to a point at the bottom of the notch.

Equations (4.11) and (4.14) can be utilized to obtain the d-spacing $d_{\phi\psi}$ (x,y) at any point on the surface of the sample. As diffraction takes place from a thin surface layer ($\simeq$ 20μm) plane stress conditions were assumed in the above calculations. The geometry of the specimen chosen for this simulation (Figure 3) also justifies the assumption of plane stress, as the notch radius is not small compared to the thickness of the specimen. Each set of values of ϕ and ψ correspond to measurement of the d-spacings in each of the three orthogonal directions. Consider for example, the d-spacing value for ϕ = 0° and ψ = 90° on surface A. This value is a result of the strain in the x direction. From equation (4.13), it can be inferred that the d-spacing measured on surface B at ϕ = 0° and ψ = 0° is a result of the strain ε_x. As the same point and thus the same set of planes are being measured on both surfaces A and B, the d-spacing resulting from the strain (ε_x in this case) ought to be the same. This is found to be true by comparing the values in Table 3. This then validates the above calculations. The results can be summarized as follows.

$$d_{0,0}^A = d_{90,0}^A$$

$$d_{0,0}^B = d_{90,0}^B \tag{4.15}$$

where the superscripts 'A' and 'B' correspond to surfaces A and B respectively. This implies that when ψ = 0, d is independent of ϕ which is seen to be true from equations (4.13) and (4.14). Also,

$$d_{0,90}^{A} = d_{0,0}^{B}$$

$$d_{90,90}^{A} = d_{0,90}^{B} \tag{4.16}$$

$$d_{0,0}^{A} = d_{90,90}^{B}$$

This equation implies that the same set of planes are being measured in both cases for the limiting conditions. The results of Table 3 are plotted in Figure 10. The different nature of the strains such as, ε_y being tensile and ε_z being compressive leads to varying slopes of the two lines in Figure 10. From Figure 10 it can be seen that the d vs $\sin^2\psi$ plots are colinear for $d_{0,\psi}^{A}$ and $d_{90,\psi}^{B}$. Similarly, they are colinear for $d_{0,\psi}^{B}$ and $d_{90,\psi}^{A}$. This is due to the fact that ε_x and ε_z are equal at the bottom of the notch i.e., at x = -0.25 in Figure 8. It can therefore be inferred that the contribution of a particular strain component plays an important role in the determination of the interplanar spacings. This is seen to be true from equations (4.11) and (4.14). As the sensitivity of the experiment is $\simeq 0.00002$ Å, the effects illustrated in Figure 10 can be detected. In this context it is worth noting that attaining precision in the x-y positioning of the x-ray beam on the specimen, particularly at the bottom of the notch, is of prime importance.

4.3 Depth of penetration calculations

X-ray diffraction techniques are confined to surface measurements. The strong attenuation due to absorption limits the depth of penetration of the x-ray beam, so that diffraction occurs from a thin surface layer of the material. The presence of a stress gradient in the near surface layers of the sample lead to a non-linearity in the d vs $\sin^2\psi$ plots discussed in the last section. This section deals with the effect of the depth of penetration on the gradient occuring on surface B of the specimen i.e, for edge measurements. To begin with, a review of the theory of absorption is given.
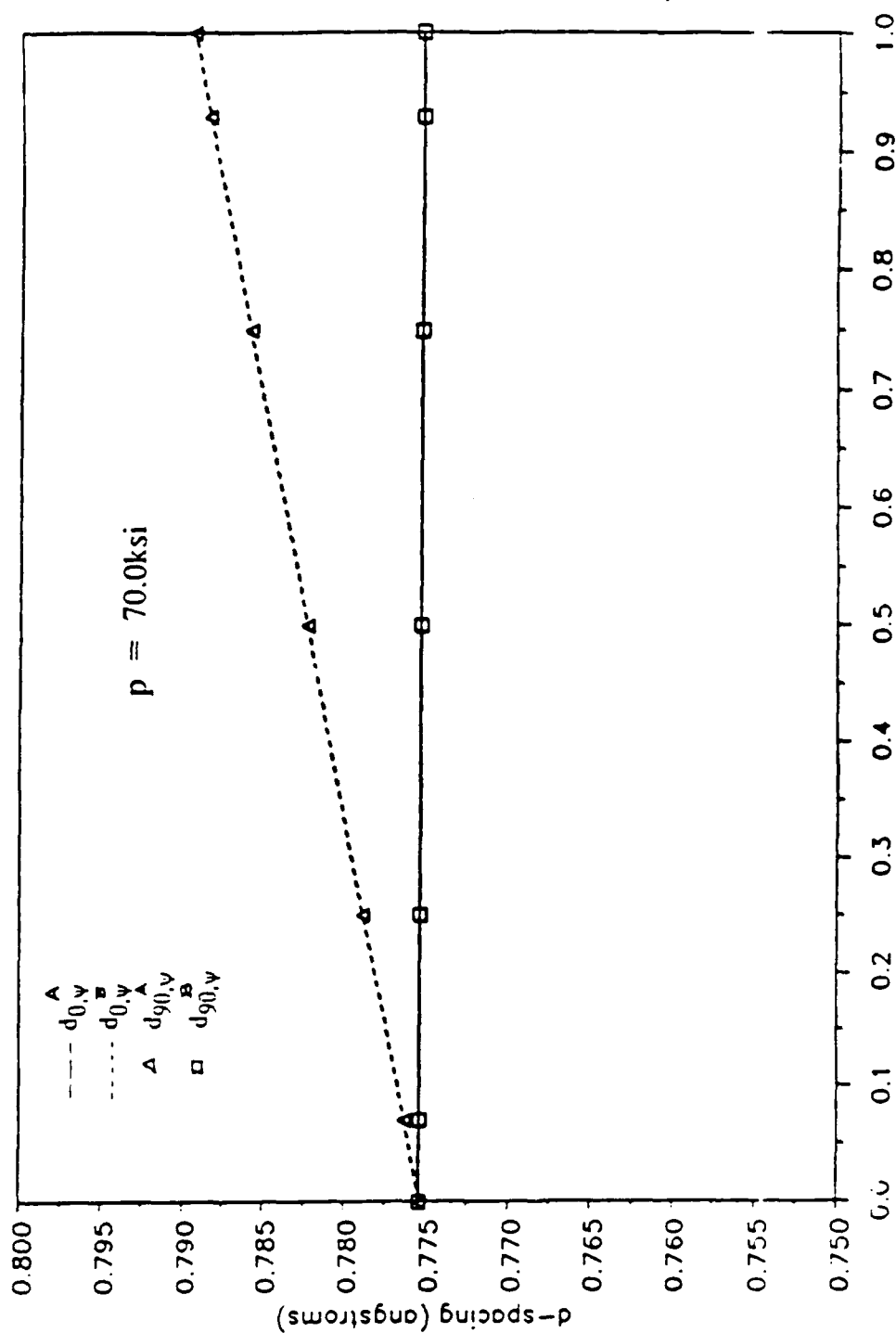
Figure 10. A plot of d vs Sin^2 ψ

4.4 Theory of absorption

In a reflection technique by x-ray diffraction, the irradiated volume that is observed includes the attenuation effect due to the absorption of the x-rays in the material. Consider an x-ray beam of cross-sectional area A_0, irradiating the surface of a sample at an angle of incidence θ. The irradiated surface area A_e is then given by,

$$A_e = \frac{A_o}{\sin \theta} \tag{4.17}$$

Figure 11 illustrates such a region. The maximum absorption is dependent on the linear absorption coefficient μ of the material. A number of sampling planes of area A_e at various distances can be imagined. Sample absorption reduces the intensity by a factor

$$exp\left[\frac{-2\mu z}{\sin \theta} \right]$$

where, μ is the linear absorption coefficient of the material and Z is the depth at which the absorption is considered. The differential intensity is then given by

$$dI_d = \frac{I_o A_o}{\sin \theta} exp\left[\frac{-2\mu z}{\sin \theta} \right] dz \tag{4.18}$$

where, I_e is the incident intensity.

If a semi-infinite slab is considered, the total diffracted intensity is obtained by integrating equation (4.18) over an infinite thickness. This intensity can be found to be

$$I = \frac{I_o A_o}{2\mu} \tag{4.19}$$
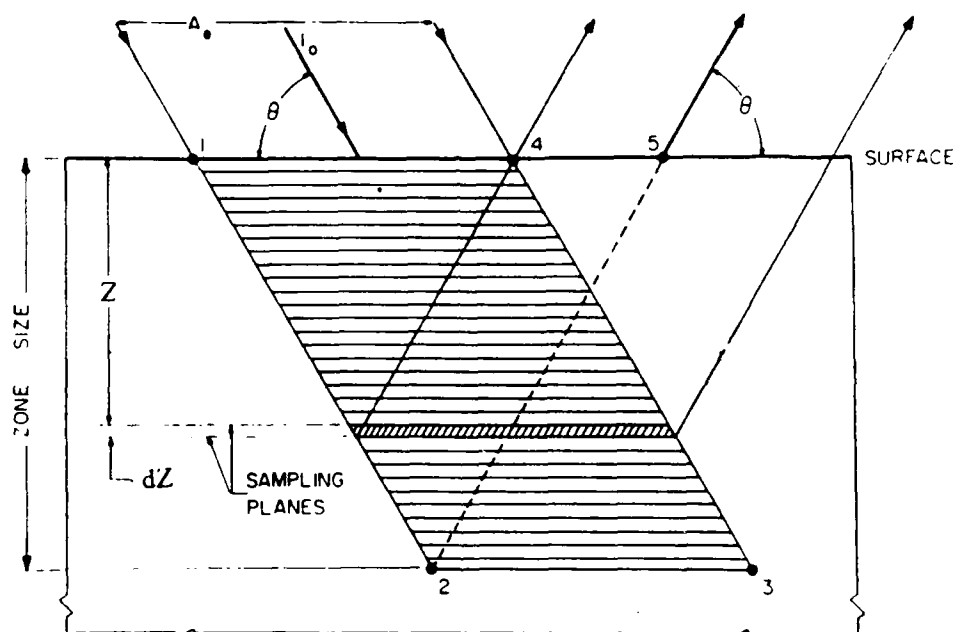
Figure 11. Cross-section of the specimen illustrating the irradiated region (Houska [31])

Here, I_c, A_c and μ are constant for all reflections and is independent of θ. The absorption factor, $1, 2\mu$, for a semi-infinite slab making equal angles with the incident and the diffracted beam, is hence found to be independent of θ. This is due to the balancing of two opposing effects. At small θ, while the specimen area irradiated by an incident beam of fixed cross-section is large, the effective depth of penetration is small. At large θ, the opposite is true. The above equations were obtained from Cullity [29].

When the specimen is tilted by an angle ψ, the resulting absorption factor is given [28] by $(1 - \tan\psi \cot\theta)$. The corresponding equation for intensity is

$$dI_d = \frac{I_o A_c}{\sin(\theta + \psi)} \cdot \exp\left[-\mu z\left[\frac{1}{\sin(\theta + \psi)} + \frac{1}{\sin(\theta - \psi)} \right] \right] dz \tag{4.20}$$

Effects due to this absorption and factors like Lorentz polarization have been taken care of in the software for the T.E.C. instrument [9].

The total intensity diffracted by a slab of material between this layer and the surface, expressed as a fraction of the total diffracted intensity is given [7] by

$$G_z = \frac{\displaystyle\int_{z=0}^{z_1} dI_d}{\displaystyle\int_{z=0}^{\infty} dI_d} = 1 - \exp\left[-\mu z_1\left[\frac{1}{\sin(\theta + \psi)} + \frac{1}{\sin(\theta - \psi)} \right] \right] \tag{4.21}$$

The effective depth of penetration maybe defined as the thickness that contributes 99% of the diffracted intensity. It is related to the linear absorption coefficient μ, ψ and the Bragg angle θ. Thus, from the above equation, for a given θ, μ and ψ, when $G_z = 0.99$, $z_1 = \delta$, where δ is the depth of penetration.

The effect of the gradient on the depth of penetration on the stress gradient is studied for measurements on the edge (surface B) of the specimen. As there is not expected to be a gradient in the

stress normal to surface A, the effect of the depth of penetration for measurements on surface A is not important.

4.4.1   Effect of the depth of penetration of x-rays

The arrangement of the specimen for edge measurement at the bottom of the notch is shown in Figure 12. The values of the depth of penetration calculated for $\psi = 0°$, where it is greatest, are listed in Table 4. This table also contains the values of the linear absorption coefficient in aluminum and titanium for two x-ray radiations [29]. The value of θ used in equation (4.21) for the calculation of δ is also given in the table.

With reference to Figure 7, and considering the greatest depth of penetration listed in Table 4, the decrease in the stress σ_y within the penetration depth is not large. Due to this stress gradient in the surface layers of the sample, the diffraction angles that are measured represent samplings of different stress values, affecting the residual stress results by a small amount. For an infinitesimal x-ray beam incident at the bottom of the notch, as in Fig. 12, and for the slit geometry being used on the TEC x-ray system, the errors encountered in the stress measurement by x-rays due to the stress gradient effect do not exceed about 2% of the measured stress value.

Another factor which affects the accuracy in stress measurements using x-ray techniques is the radius of curvature of the sample. This effect was studied for two different notch radii, for both aluminum and titanium specimens. The results of this study are shown in Appendix A.1. The error in the stress values due to varying radius of curvature was found to be of the order of 2 ksi, for any value of measured stress. For the counting statistics available on the TEC system, this error is of a very small magnitude. Hence, this effect is not of importance for measurements made using the TEC x-ray system.
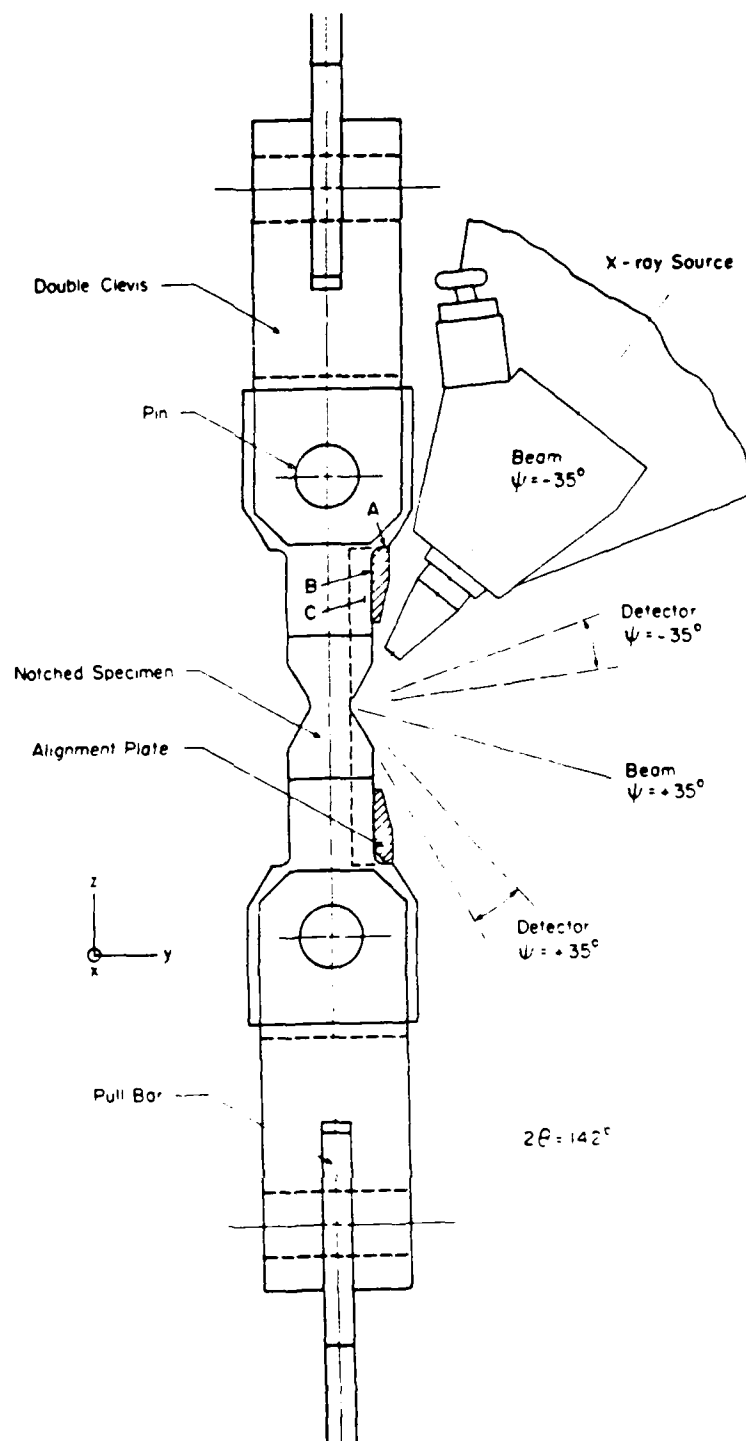
Figure 12. Arrangement for measurements on the edge of the specimen.

Table 4. Values of the depth of penetration in Al and Ti for two different radiations used.

(a) Radiation : CuK$_a$ at $\psi = 0°$

Materials	Planes	2θ, deg	μ, cm^{-1}	δ, 10^3 in, for absorption of:	
				95%	99%
Al	(511/333)	162.5	131.5	4.43	6.81
Ti	α — hcp (213)	139.5	926.2	0.597	0.918

(b) Radiation: CrK$_a$ at $\psi = 0°$

Materials	Planes	2θ, deg	μ, cm^{-1}	δ, 10^3 in, for absorption of:	
				95%	99%
Al	(311)	139.2	402.3	1.37	2.11
Ti	α — hcp (201)	136.3	2737.6	0.200	0.296
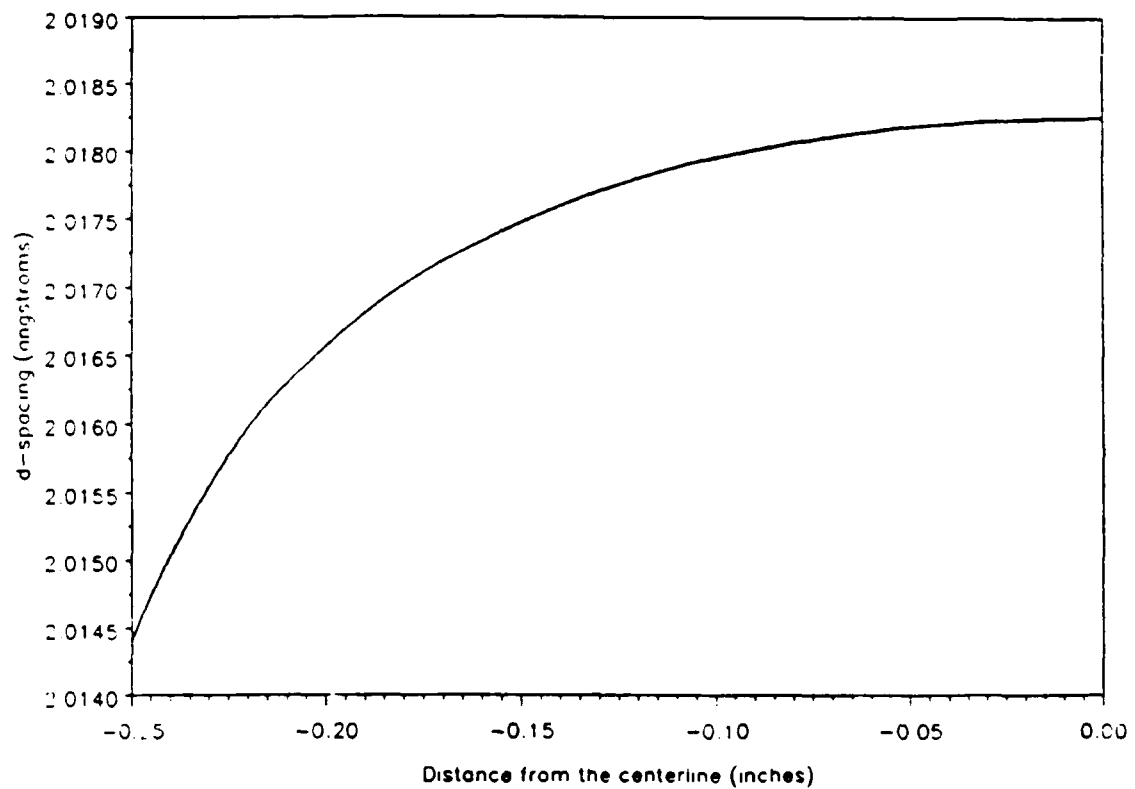
Figure 13.   d-spacing for (200) plane, 7475 Al, using CuKα, at $\psi = 0$, as a function of distance from the centerline.
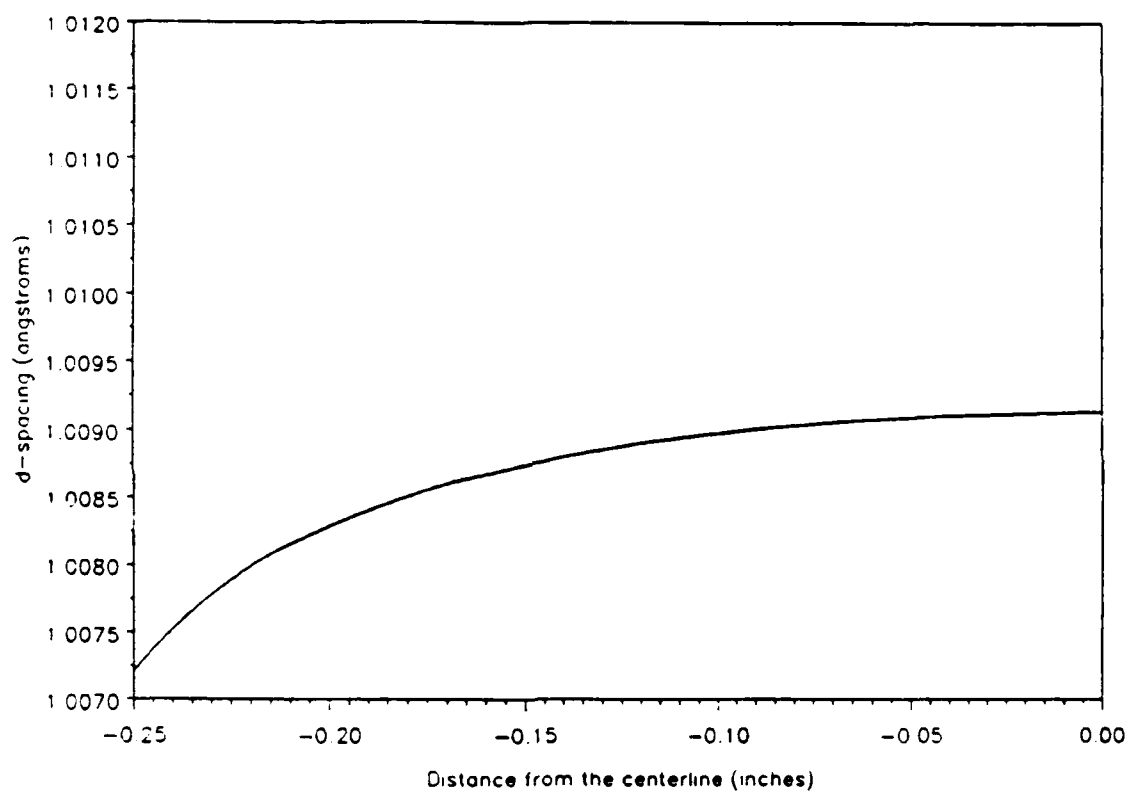
Figure 14.   d-spacing for (400) plane, 7475 Al, using CuKα, at $\psi = 0$, as a function of distance from the centerline.
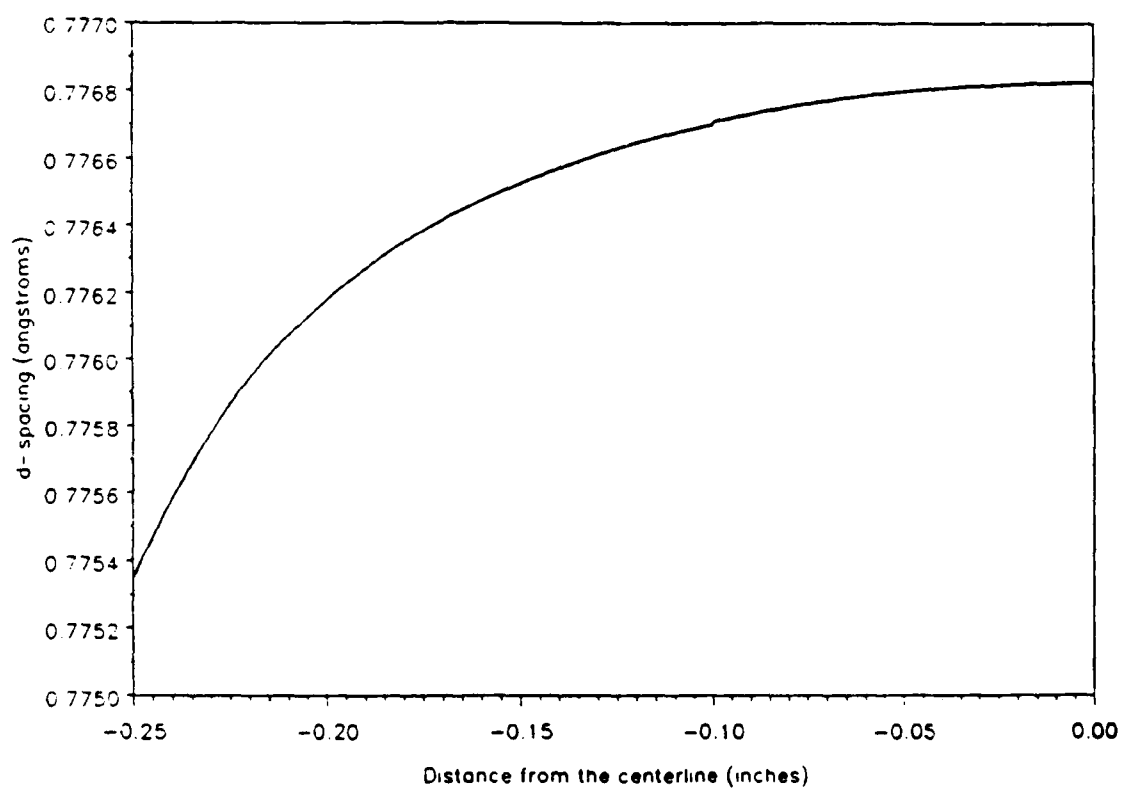
Figure 15.   d-spacing for (333) plane, 7475 Al, using CuKα, at $\psi = 0$, as a function of distance from the centerline.

4.5 d-spacing calculations

The strain distribution illustrated in Figure 8 was used to obtain the d-spacing variation as a function of the distance from the centerline. This was done for a 7475 Al specimen using CuKα radiation. This profile was used primarily to simulate the line profile on the flat surface (A) of the notched specimen. Details regarding this simulation are described in this chapter. As the x-ray response in terms of the line profiles was studied on the flat surface of the specimen, the d-spacing profiles were also obtained for the same surface.

Consider an x-ray beam incident on surface A of the specimen as shown in Figure 3. The interplanar spacing d of the diffracting planes parallel to the surface, result from the strain normal to the surface. This strain for $\psi = 0$ is the strain in the z direction, i.e., ε, or ε_{33}. The d-spacing profiles for three orders of reflections namely (200), (400) and (333), resulting from ε, strain are illustrated in Figures 13-15. The value of d_0 for these reflections, were obtained from Pearson's Handbook [26]. These profiles were obtained from the strain distribution of Figure 8 and equation (4.02). Figure 13 exhibits a gradient which is steep in the region close to the notch and decreases gradually to zero at the largest distance away from the notch. This can be attributed to the direct proportionality of the d-spacing with the strain, which displays a similar behavior (Figure 8).

4.6 Simulation of intensity profiles

4.6.1 Introduction

The most common kind of data one obtains from a diffractometer is a graph showing the variation of the diffracted intensity as a function of 2θ. Theoretically the diffracted intensity is defined to be a step function. However in reality, factors like the presence of a mosaic structure (small regions slightly misoriented from one another) in the crystal, size of the crystal, presence of nonuniform elastic stresses and strains and instrumental effects may lead to a broadening of the diffracted intensity. Such a broadened diffracted intensity is known as a line profile.

This section describes the simulation of intensity or line profiles resulting from the d-spacing profiles illustrated in Figures 13, 14 and 15. The simulation was carried out for an x-ray beam incident on surface A of the notched specimen (Figure 3). Intensity profiles were simulated for diffraction from each grain in the region between the notches, for a beam of finite size. The profiles were simulated to study stress gradient effects, and thus, the effects of a non uniform macrostrain on surface A of the specimen. The same simulation was not done for surface B at the bottom of the notch. This is because, for surface B, for a finite beam size used in the simulation (and also in the experimental work), the strain gradient relative to the depth of penetration of the x-ray beam (discussed in section 4.3) is negligible. Hence, the effect of this gradient on the line profile would be insignificant. All the results presented in this section were obtained by running the simulation for a 7475 Al notched tensilr specimen.

4.6.2 Theory

The d-spacing profiles from figures 13-15 were used in the simulation of the intensity profiles. The intensity profiles corresponding to the d-spacing variations were generated using a computer routine written specifically for this purpose. It should be noted that the strain distribution used as the basis for these calculations corresponds to $y = 0.0$, ie., along the centerline of the notches. The variation in the stress distribution between $y = 0.0$ and 0.1 has already been shown to be small (Figure 7).

The 2θ values corresponding to the d-spacings calculated in the last section can be computed from equation (2.01) as

$$\theta = \sin^{-1}(\frac{n\lambda}{2d})$$ (4.22)

The continuous variation of the d-spacing gives rise to an intensity profile spread over a 2θ range according to Bragg's law. However, the simulated profile includes broadening due to the sample and the instrument. This can be accounted for by the use of a Pearson-VII [30] function. This function can be used widely for fitting profiles of Cauchy and Gaussian shapes, including the modified Lorentzian shape. The P-VII, as it is usually called, is given by,

$$Y = Y_o\left[1 + \frac{(2\theta - 2\theta_o)^2}{ma^2} \right]^{-m}$$ (4.23)

where, the parameters Y_e and $2\theta_o$ indicate the intensity and the position of the peak. The integral of (Y) with infinite limits with respect to θ is normalized if

$$Y_o = Y_n = \frac{(\pi m)^{-1/2}}{a} \frac{\Gamma(m)}{\Gamma(m - 1/2)}$$ (4.24)

where, 'a' and 'm' are two adjustable parameters that describe the peak shape and the width respectively. The full width at half maximum (FWHM) can be shown to be

$$W = 2a\left[m(2^{1/m} - 1) \right]^{1/2} \tag{4.25}$$

When m = 1,2 and ∞, the P-VII becomes a Cauchy, modified Lorentzian and Gaussian curve respectively.

In order to obtain a smooth variation in the intensity profile, the d-spacing profile calculated from the strain distribution was expressed as a series of five polynomials. This five segment approximation of the d-spacing profile is shown in Figure 16. The five segment approximation corresponding to the higher order reflections are also shown in Figures 17 and 18.

4.6.3   Intensity profile calculations

A computer simulation approach to obtain composition profiles has been done earlier in diffusion studies by Houska and co-workers. This has been reviewed in an article by Houska [31]. In the approach by Houska, the variation of the composition and depth was considered. However, in the present model, as the d-spacing variation with depth is negligible, the d-spacing variation along the x-axis, as opposed to depth, was considered.

A computer program was written to calculate the intensity profiles. The program used as input the d-spacing of the planes in the unstressed state (d_o) for the specific reflections considered which in the present case were (200), (400) and (333). The height above the centerline of the notches, y, at which the stress distribution had to be determined was also input into the program. The program is capable of determining the stress distribution and the line profiles for different values of y. However, the intensity profiles have been illustrated for a y value of 0.0 only. The other inputs correspond to the coefficients of the polynomial equations used in the five segment approximation of the d-spacing profile. Sample input files are shown in Appendix B.
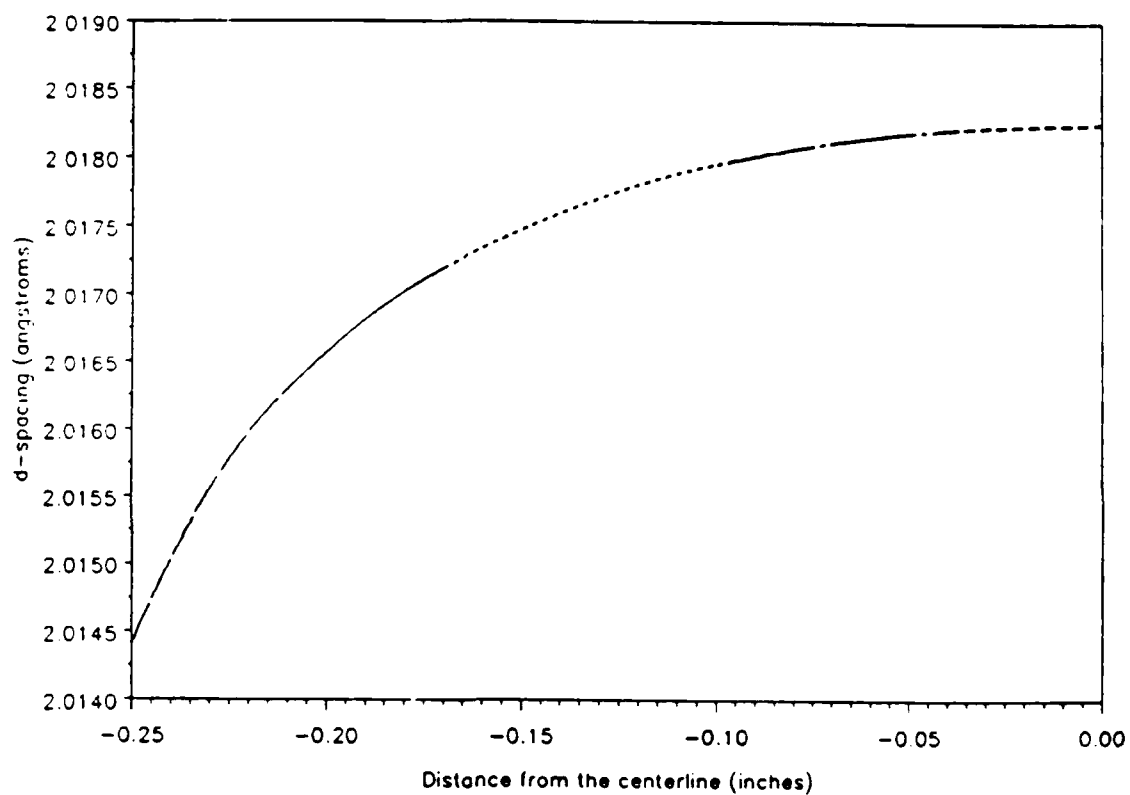
Figure 16. Five segment approx of d-spacing for (200), 7475 Al, CuKα, at $\psi = 0$ as a function of distance from the centerline
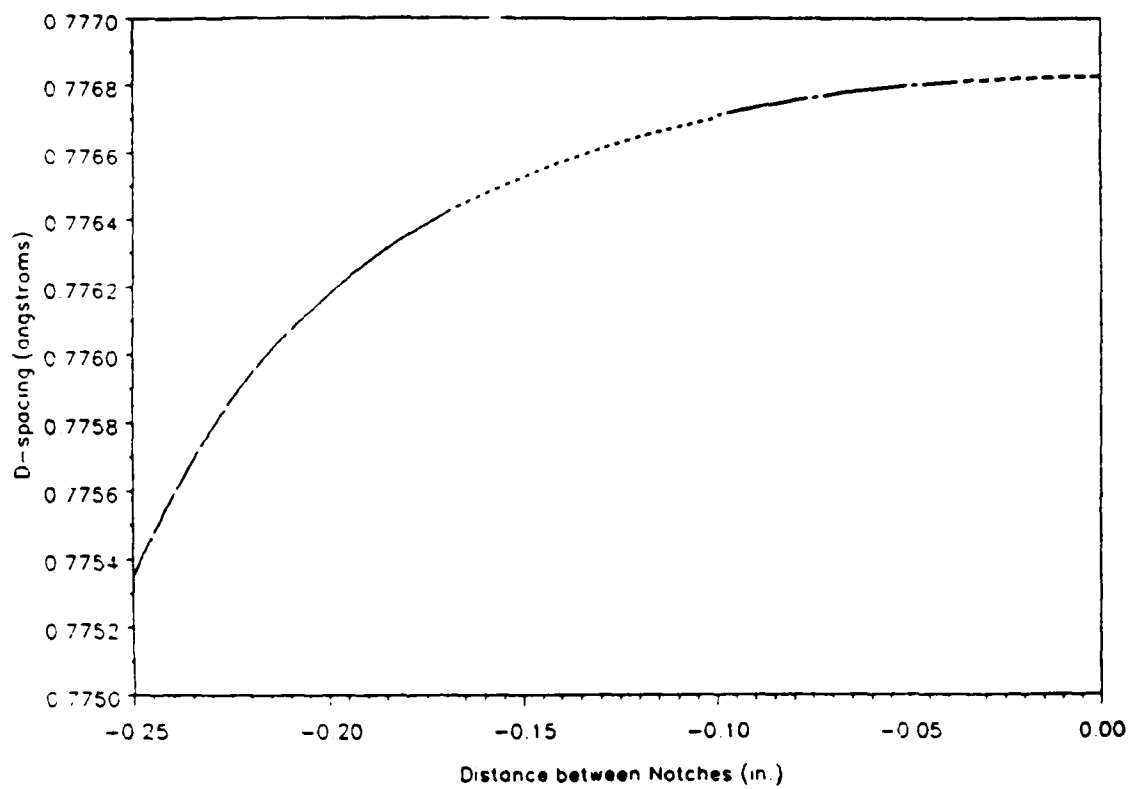
Figure 17.   Five segment approx of d-spacing for (400), 7475 Al, CuKα, at $\psi = 0$ as a function of distance from the centerline
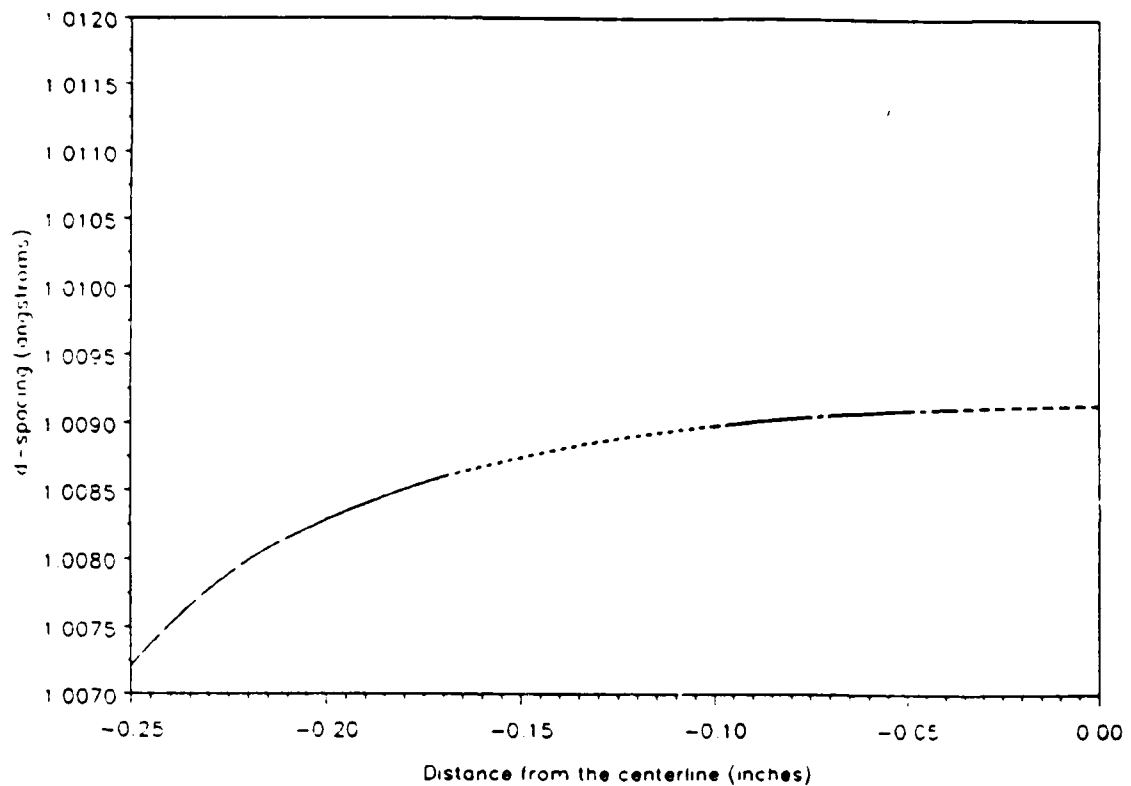
Figure 18.   Five segment approx of d-spacing for (333), 7475 Al, CuKα, at ψ = 0 as a function of distance from the centerline

The program is divided into the following four sections :

- The main program calculates the intensity profile.

- Subroutine STRAIN calculates the stress and strain values using the equations presented in chapter 3.

- Subroutine DX2TT calculates the d-spacing variation.

- Subroutine DVSSIN calculates the d vs $\sin^2 \psi$ values for the model developed earlier.

The main program first divides the representative area, which in this case is the region along the centerline of the notches, into many fine strips along the x-axis. As the d-spacing gradient in each strip is of a small magnitude, the d-spacing in each fine strip is approximated as a constant. The intensity for each strip was first calculated. This intensity was broadened using the Pearson VII function (equation 4.23). The broadened intensity was then superimposed, by means of a summation loop, to obtain the simulated intensity profile. This summation is a summation of intensities. For the sort of summation done in the present situation, the coherence length of the subgrain was assumed to be small. The depth of penetration, d-spacing gradient and the subgrain size of the material are factors which affect the calculations. The depth of penetration of a CuKα radiation in Al has already been found to be small (Table 4). For this depth of penetration, the variation in the d-spacing due to the strain ε, is small. These two factors and the assumption of a small subgrain size help in justifying the summation of intensities in our calculations. The intensity profile based on the above calculation is shown in Figure 19. The program was then run for higher order reflections, namely, (400) and (333). The profiles generated for these are also illustrated (Figures 20-21).

Broadening observed in any intensity profile is actually a convolution of four different broadening functions. These are : broadening due to non-uniform strain, dislocation strain broadening, particle size broadening and instrumental broadening. The intensity profiles illustrated in Figures (19-21) depict a clear asymmetry. In order to know the contribution of each of the broadening function towards the asymmetry, a line shape analysis of the profiles is required. As the method by which

the intensity profile was generated, is a linear summation over a series of fine strips along the x-axis, information of the kind required in the present situation can be obtained, by plotting the results due to the summation over a smaller range. This result is shown in Figure 22. In this case, half the region between the notches was divided into approximately 1200 linear elements and the intensity due to each element was obtained from the computer program. Each peak was then broadened using the Pearson VII function discussed earlier in this chapter. The linear elements were then summed twice. The results were first summed over the entire region between the notches (Figure 3), to generate the profile revealing the asymmetry in Figures 19, 20 and 21. The second summation was over separate regions, which covered one tenth the region between the notches along the notch centerline on the flat surface (A), each of which is equivalent to the width of the slit, 0.5mm (0.02"), used in the TFC x-ray system. Looking at the profiles generated by these ten segments (Figure 22), it is clear that the profile with the maximum peak corresponds to the region farthest away from the notch, and thus, a low strain gradient. As each peak corresponds to a normalized distribution function, the area under the curve is taken to be a constant.

4.6.4 Discussion of the intensity profiles

The intensity profiles were found to be very sensitive to variations in the d-spacings, ie., to the d-spacing gradient. Small variations in the inter-planar spacings lead to large changes in the slope, which give rise to large changes in the shape of the intensity profile. With reference to Figure 19, the peak of the intensity profile is found to correspond to a small d-spacing gradient. This is because, for low gradients, the x-ray beam covers a larger region of material and thus a greater number of grains. It should be noted that the profiles simulated here correspond to a d-spacing variation along the x-axis, on surface A (Figure 3) of the specimen. The d-spacing at each position along the x-axis is a result of the strain in the z direction and thus for $\psi = 0$. Hence, for this simulation, the absorption for each element along the x-axis of the x-rays incident on surface A was assumed to be constant.
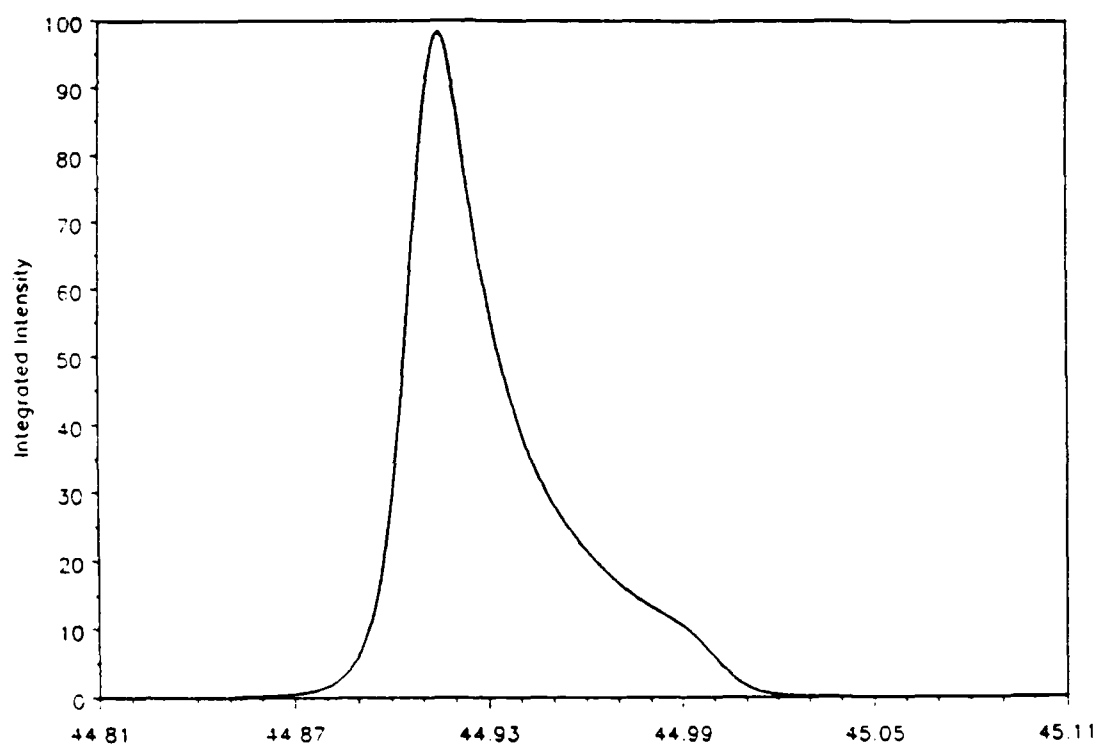
Figure 19. Intensity profile for (200) plane, 7475 Al, using CuKα radiation through a rectangular slit.
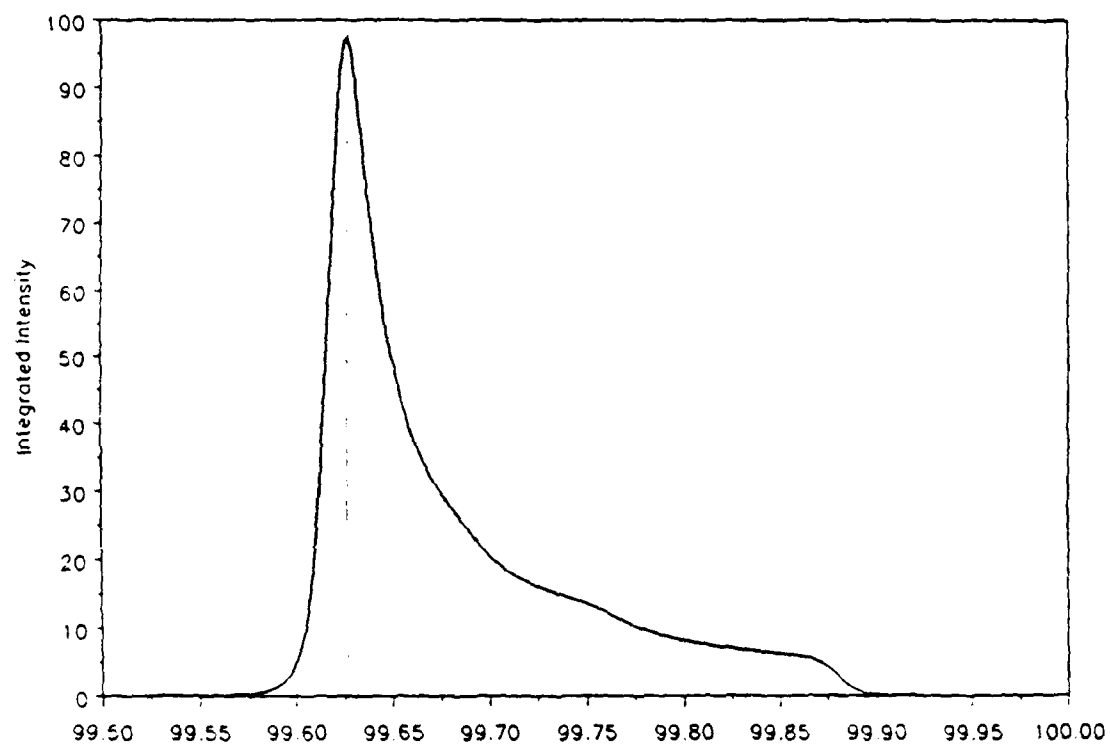
Figure 20.   Intensity profile for (400) plane, 7475 Al, using CuKα radiation through a rectangular slit.
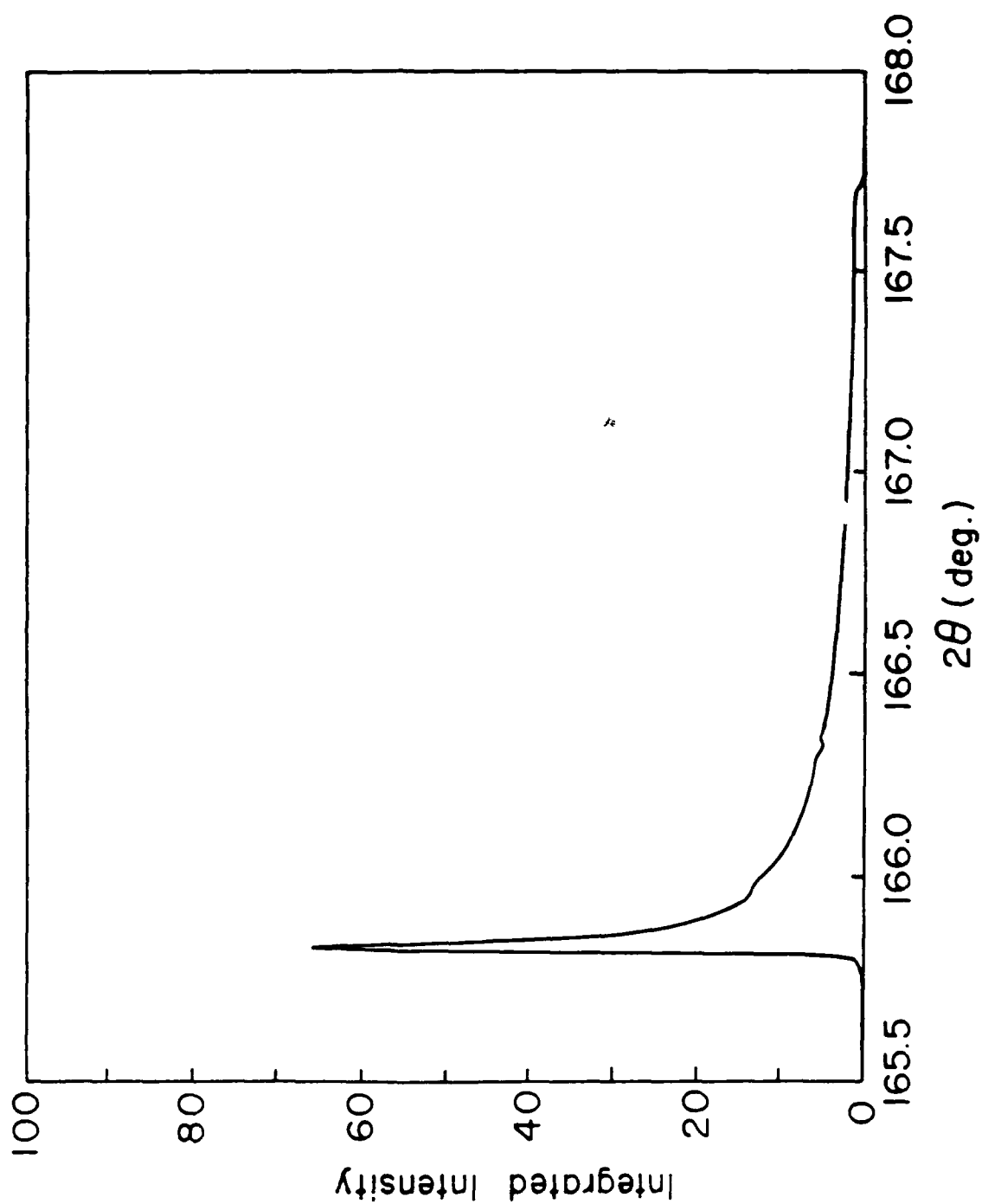
Figure 21. Intensity profile for (333) plane, 7475 Al, using CuKα radiation through a rectangular slit.
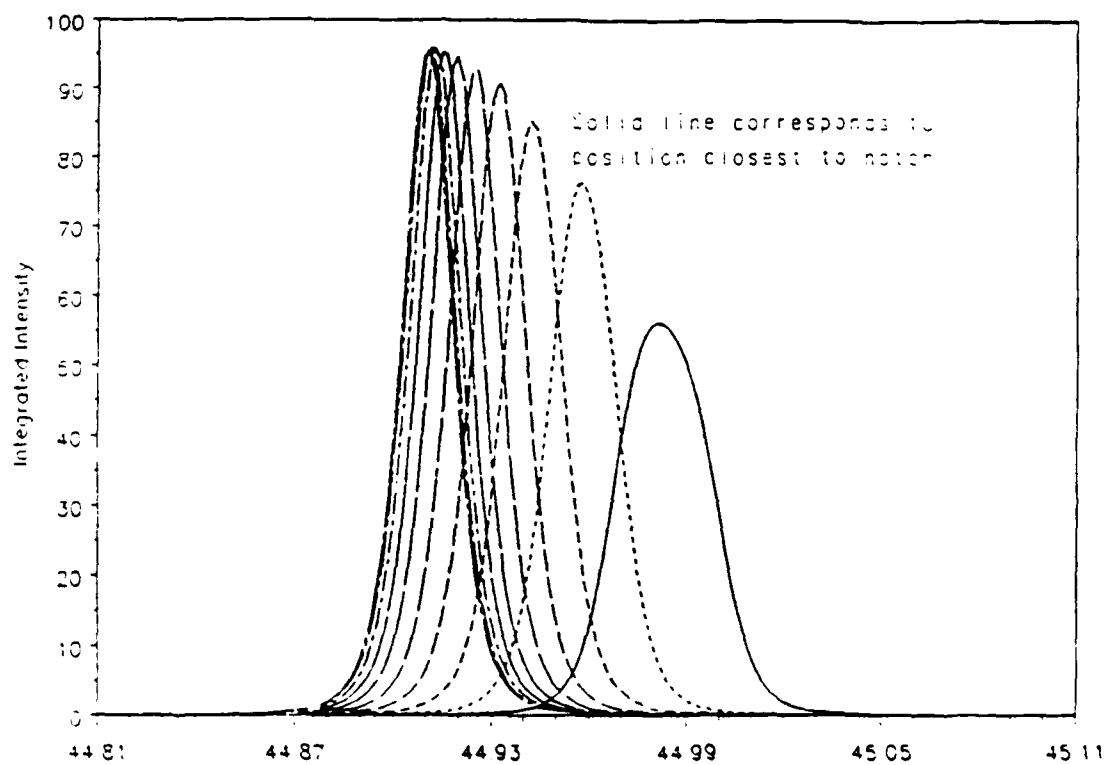
Figure 22.   Intensity profile for (200) plane, 7475 Al, using CuKα, from ten segments, each
segment of width 0.02".

In the calculation of the intensity profiles, as stated earlier, the region in between the notches on surface A was divided into a number of strips. The size of the strip used in the computation was small compared to the grain size of the material. The depth of penetration of the x-ray beam was found to be small too (refer Table 4). The coherence length of a subgrain which in this case is the column length, is assumed to be small for this depth of penetration. The profiles shown in Figures 19-21 were obtained by summing up the intensities from each column. The asymmetry in the profile is best understood by treating each domain in the region between the notches on surface A in terms of a column of cells.

Consider a column of cells as illustrated in Figure 23 wherein, a_1, a_2 and a_3 are the directions along the cell edges. Each domain can be expressed in terms of a column of cells along the a_3 direction, perpendicular to the reflecting planes. i and i' represent different columns. From the expression for integrated intensity [32], it is seen that contributions to the intensity are only from pairs of cells for which $m_1' = m_1$ and $m_2' = m_2$. This implies that there is no contribution to the integrated intensity in each column due to cross-over terms. In other words, cells from different columns do not contribute to the integrated intensity in each column. As the x-ray beam not only scans all columns in a single grain or subgrain, all other grains having similar orientations also contribute towards the intensity profile. The intensity profiles obtained by the simulation have been by a superposition of the intensities from different columns and subsequently from different grains.

This theory for the calculation of the intensity relating to a column of cells is for a characteristic d-spacing. The program calculates the intensity for a group of cells in the domain corresponding to a particular d-spacing. Different groups of cells over the domain lead to a variation in the d-spacing. The overall profile is obtained by a summation over all the groups of cells in the entire domain.

The profiles corresponding to the lower order reflections depict a very narrow 2θ range. The profile for the (333) reflection shows a 2θ range of approximately 2°. The variation in this profile is considerably sharp, with the predominant contribution to the asymmetry being from the tail portion.
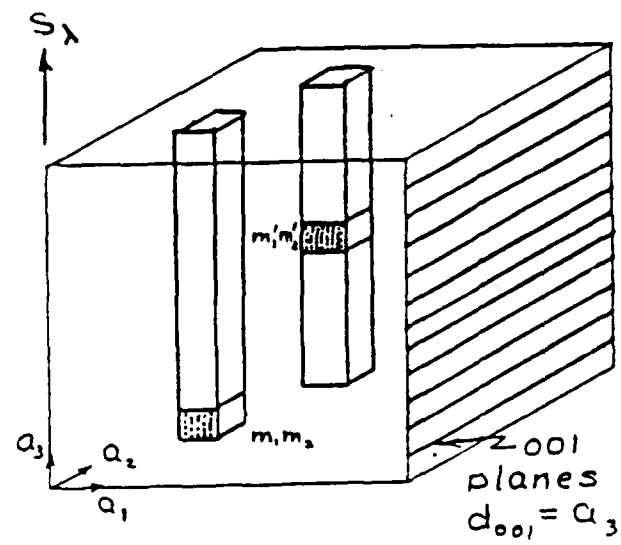
Figure 23.   A crystal showing a column of cells (Houska [35]).

The effects of the intensity profiles may not be easily measurable on the TFC x-ray system being used in the experimental work. They can however be measured on an x-ray diffractometer with a higher resolution using a $K\alpha_1$ monochromator.

Consider the simulated profiles illustrated in Figures (19-21). These profiles are plotted for three different orders of reflection (hkl). For higher orders of reflection, the inter-planar spacing decreases according to the equation,

$$d = \frac{a}{\sqrt{h^2 + k^2 + l^2}} \qquad (4.26)$$

where a is the lattice parameter of the material from which diffraction occurs. Higher order of reflections correspond to a lower d value and hence a larger 2θ, as, the inter-planar spacing and θ have an inverse dependence (Bragg's Law).

The peak shape depends on the size of the source, finite divergences of the slits at the x-ray tube and the receiving slits, and the fact that, in a diffractometer, a flat specimen is tangent to the focussing circle at only one point. All x-ray measurements on the TFC x-ray system are on the high angle side. At high angles, all the above factors become less important. Also at high angles, the resolution in $\Delta\theta$ is larger compared to the resolution at low angles. This is evident from equation 2.02b which is

$$\Delta\theta = -\frac{\Delta d}{d_{hkl}} \tan\theta = -\varepsilon \tan\theta$$

These high angle measurements are confined to a 2θ range of $140° - 170°$. The profile for (333) reflection is for a high angle diffraction, i.e., $2\theta \simeq 160°$. This profile shows an asymmetry over a 2θ range of $2°$. The profiles for (200) and (400) are for diffraction at a 2θ of $\simeq 45°$ and $90°$ respectively.

71

In an actual experimental measurement, a broadened intensity profile of a form similar to Figures (19-21) is obtained. The broadening due to the instrument can be obtained from measurements on a well annealed sample. Measurements made on a sample with very few defects, using a system whose instrumental broadening is known, yields the sample or particle size broadening. A measured profile is usually from a deformed sample in a real instrument. This profile is a convolution of the the broadenings due to the sample and the instrument, and also the effects due to a non-uniform macrostrain. The broadening due to the non-uniform macrostrain can be determined, if the factors due to the sample and the instrument are known.

From the experiments done on the TEC x-ray system, the Full Width at Half Max (FWHM) for diffraction on Aluminum specimens was $\simeq 2^\circ - 3^\circ$. The FWHM is really a measure of the resolution of the instrument. Considering the fact that one of the effects exhibited by the simulation is of the same order $\simeq 2^\circ$ the effect may be measurable experimentally, but with some difficulty. This effect should be easily measurable on a diffractometer with a higher resolution.

5.0 Conclusions and Recommendations for Future Work

Based on the results of the analytical model, the following conclusions can be drawn.

- Calculations related to the stress distribution model for an infinite specimen can be extended to a specimen of finite geometry. The error encountered due to this approximation is of the order of 3 percent.

- The calculations regarding the variation of the inter-planar spacing with the ψ angle, illustrated as a plot of d vs $\sin^2\psi$, can be used as a basis for experimental measurements. The variation in the interplanar spacing are easily measurable experimentally. The tabulated values, calculated for a point at the notch tip, can be verified experimentally. In this context, attaining precision in the x-y positioning of the x-ray beam on the specimen, is of prime importance.

- A study of the effect of the depth of penetration of the x-ray beam on the stress gradient occuring on the surface reveals that residual stress measurements are feasible along the edge of the specimen.

- The intensity profiles simulated are due to the strain gradient on the surface. They are a result of a non-uniform macrostrain in a notched specimen subjected to tensile loading.

6.0 References

1. Mathar, J., Determination of Initial Stresses by Measuring the Deformation Around Drilled Holes, Trans. ASME, 1934, 56(4), pp.249-254.

2. Crecraft, D.I., Ultrasonic Measurement of Stresses, Ultrasonics, 1968, April, pp.117-121.

3. Gardner, C.G., Barkhausen Noise Analysis, Proc. of a Workshop on Nondestructive Evaluation of Residual Stress, NTIAC-76-2, 1975, pp.211-217.

4. Lester, H.H., and Aborn, R.M., Army Ordnance 6, 120, 200, 283, 364 (1925-1926).

5. Nye, J.F., Physical Properties of Crystals, Oxford University Press, Oxford, Great Britain, 1976.

6. Hilley, M.E., Ed., Residual Stress Measurement by X-Ray Difraction, SAE Information report, J784a, Society of Automotive Engineers, New York, 1971, Aug., pp.3-16.

7. Noyan, I.C., and Cohen, J.B., Residual Stress Measurement and Interpretation, Springer - Verlag. (1987).

8. Prevey, P.S., A Method of Determining the Elastic Properties of Alloys in Selected Crystallographic Directions for X-Ray Diffraction Residual Stress Measurement, Adv. in X-ray Anal. 1977, vol.20, 345-354.

9. TEC model 1600 X-ray Stress Analysis System Operation and Maintenance Manual, Technology for Energy Corp., Knoxville. TN, 1985.

10. Kelly, C.J., and Eichen, E., Computer Controlled X-Ray Diffraction Measurement of Residual Stress, Advances in X-ray analysis, 1972, vol.16, pp.344-353.

11. Weinamn, E.W., Hunter, J.E., and McCormack, D.D., Determining Residual Stresses Rapidly, Metals Progress,1969, July pp.88-90.

12. Koves, G., and Ho, C.Y., Computer Automated X-Ray Stress Analysis, Norelco Reporter, 1964, vol II, pp.99-103.

13. Hendricks, R.W., One-and Two-Dimensional Position-Sensitive X-ray and Neutron Detectors, Tr. Am. Cryst. Assoc., 1976, 11, p.125.

14. James, M.R., and Cohen, J.B., PARS - A Portable X-Ray Analyzer for Residual Stresses, Journal of Testing and Evaluation, 1978, vol.6, March, No.2, pp.91-97.

15. James, M R., An Examination of Experimental Techniques in X-Ray Residual Stress Analysis, Ph D Thesis, Northwestern Univ., Evanston. Illinois, 1977.

16. James, M R , and Cohen, J B., Application of Position Sensitive Detector to the Measurement of Residual Stresses, Adv X-ray Anal., 1976, vol 19, pp 695-708

17. James, M.R., and Cohen, J.B., Study of the Precision of X-Ray Stress Analysis, Adv. X-ray Anal., 1977, vol.20, pp.291-308.

18. James, M.R., and Cohen, J.B., Geometrical Problems with a Position Sensitive Detector Employed on a Diffractometer, Including its Use in the Measurement of Stress, J. Appl. Crystall, 1979, vol.12, pp.339-345.

19. Dowling, N.E., and Ranganathan, K., Residual Stress Measurements in Notched Test Specimens Using X-Ray Diffraction, paper submitted to the ASTM journal of Testing and Evaluation, Virginia Polytechnic Institute and State University, Blacksburg, Virginia, 1987, May.

20. Neuber, H., Kerbspannungslehre, 2nd ed., Springer, Berlin (1959), Translation, Theory of Notch Stresses, AEC-tr-4547, 1961.

21. Peterson, R.E., Stress Concentration Factors, John Wiley and sons Inc., New York, 1974.

22. Kikukawa, M, A Note on the Stress Concentration Factor of a Notched Strip, Proc. 3rd Congr. on Theoretical and Appl. Mech., Bangalore, India, 1957, pp.59-64.

23. Kikukawa, M., On Plane Stress Problems in Domains of Arbitrary Profiles, Proc 4th Japan Natl. Congr. for Apl. Mech., 1954, pp.149-152.

24. Flynn, P.D., and Roll, A.A, A Re-examination of Stresses in a Tension Bar with Symmetrical U-shaped Grooves, Proc. Soc. Exp. Stress Analysis, 1966, vol.23, Pt 1, p.93.

25. Byars, E E., and Snyder, R.D., Engineering Mechanics of Deformable Bodies, International Textbook Company, Scranton, 1969, p.558.

26. Pearson, W.B., A Handbook of Lattice Spacings and Structures of Metals and Alloys, 1967, vol 1, p 346

27. Dölle, H., The Influence of Multiaxial Stress States, Stress Gradients and Elastic Anisotropy on the Evaluation of Residual Stresses by X-rays, J. Appl. Cryst., (1979), 12, pp.489-501

28. James, M.R., The Measurement of Residual Stresses by X-Ray Diffraction Techniques, Treatise on Materials Science and Technology, vol. 19A.

29. Cullity, B.D., Elements of X-ray diffraction, Addison-Wesley Publishing Company Inc., Reading, MA, 1956, p.466.

30. Naidu, S.V.N., and Houska, C.R., Profile Separation in Complex Powder Patterns. J. Appl. Cryst., 1982, 15, pp. 190-198.

31. Houska C.R., The Investigation of Composition Variations by Diffraction. Treatise on Materials Science and Technology, Experimental Methods, (edited by H.Herman),Vol. 19A, P. 63, Academic Press N.Y. (1980).

32. Warren, B.E., X-Ray Diffraction, Addison-Wesley Publishing Company Inc., Reading, MA, 1969, pp. 264-269.

33. Hendricks, R.W., to be published.

34. Hendricks, R.W., private communication. Virginia Polytechnic Institute and State University, Blacksburg, Virginia.

35. Houska, C.R., private communication. Virginia Polytechnic Institute and State University, Blacksburg, Virginia.

THIS PAGE INTENTIONALLY LEFT BLANK

THIS PAGE INTENTIONALLY LEFT BLANK

Appendix

Effect of the radius of curvature of the sample on the error in d-spacings

For a sample with a radius of curvature r_s the total shift in the centroid of the diffraction peak has been found to be

$$\Delta 2\theta = -\frac{2}{3}\frac{r_{gc}}{r_{pspc}}\frac{\alpha^2 \sin^2\theta}{\sin^2(\theta + \psi)}\left[1 + \frac{r_{gc}(1 - \alpha)^2}{2r_s \sin(\theta + \psi)}\right] \qquad (A - 1)$$

where r_{gc} is the radius of the goniometer circle with the center on the point where the x-ray beam strikes the sample and passes through the x-ray tube focal spot, r_{pspc} is the distance between the centers of the goniometer and the detector, the detector being parallel to a tangent of the goniometer circle, θ is half the Bragg angle, r_s is the radius of curvature of the sample, and α is half the angular beam divergence. Note that convex samples have $r_s > 0$ and concave samples have $r_s < 0$. The angular beam divergence for a point source and a source of finite height is shown in Figures A-1(a) and A-1(b) respectively, in which d is the width of the slit, u is the distance between the two apertures, v is the distance of the exit pinhole from the source, h is the height of the source, and $2\alpha_1$ and $2\alpha_2$ are the maximum angles of divergence for the two cases.
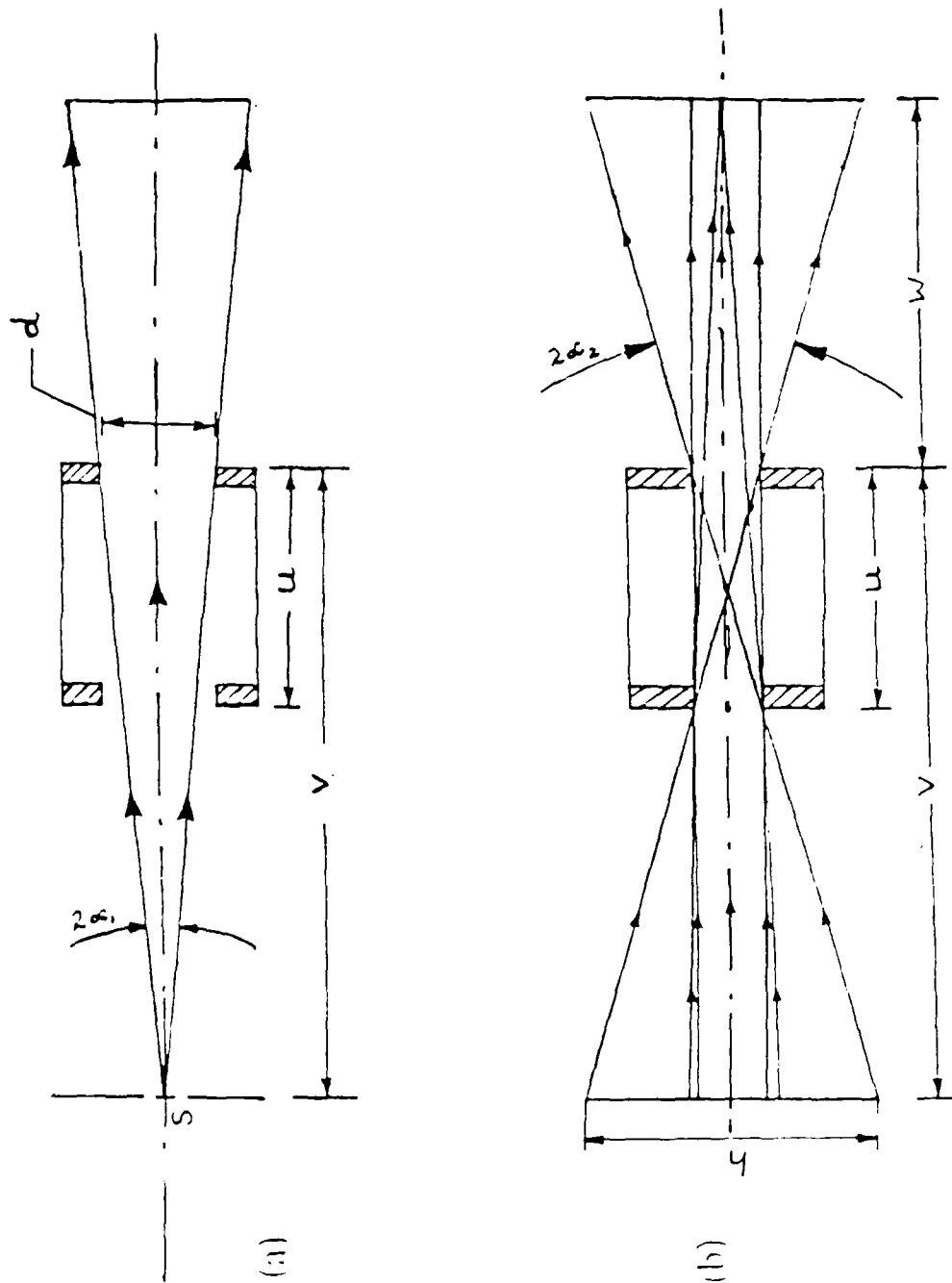
Figure A-1. Angular divergence for (a) point source and (b) source with a finite height.

The source pertaining to the present investigation is square in shape with 'h' approximately being equal to 2 mm (Figure A-1(b)). The divergence in radians is then given by,

$$\alpha_2 = \frac{(d/2)}{(u/2)} = \frac{d}{u}$$

Hence,

$$\alpha = \frac{d}{u} \qquad\qquad (A - 2)$$

Using equation (A-1) and differentiating equation (2.01) and solving, the error in the d-spacing is,

$$\frac{\Delta d}{d} = \frac{2}{3} \frac{r_{gc}}{r_{pspc}} \frac{\alpha^2 \cos^2\theta}{\sin^2(\theta + \psi)} \left[1 + \frac{r_{gc}(1 - \alpha)^2}{2 r_s \sin(\theta + \psi)} \right] \qquad (A - 3)$$

Equation (A-3) shows that the shift in d-spacing involves a term which is inversely proportional to the radius of curvature of the sample. Substituting the following known values for the diffractometer being used in the experimental work, i.e.,

d = 0.5mm,

u = 50mm,

α = 0.01 radians = 0.6°,

r_{gc} = 200mm and

$\frac{r_{gc}}{r_{pspc}} \simeq 1$

Eq. (A-3) becomes,

$$\frac{\Delta d}{d} = 6.67 \times 10^{-5} \frac{\cos^2\theta}{\sin^2(\theta + \psi)} \left[1 + \frac{98.01}{r_s \sin(\theta + \psi)} \right] \qquad (A - 4)$$

The values of $\frac{\Delta d}{d}$ in parts per million for different ψ angles corresponding to each of the 2θ bracket used are shown in Table A-1. Equations (A-1) and (A-4) presented here are derivations by Hendricks [33]

Table A-1. Estimate of the error in d-spacing values for differing radius of curvature.

Radius of curvature	Material	$\frac{\Delta d}{d}$ (ppm)				
		$\psi = 0°$	10°	20°	30°	45°
3.175mm	Al[1]	-62.9	-60.0	-62.9	-72.5	-109.9
	Ti[2]	-250.1	-219.1	-211.2	-223.3	-291.7
6.35mm	Al	-30.4	-29.0	-30.4	-35.1	-53.5
	Ti	-121.1	-106.0	-102.0	-108.0	-141.5

[1] $2\theta = 160°$ and [2] $2\theta = 142°$

These values have been calculated for two different radii of curvature, $r_s = -3$ mm and $r_s = -6$ mm respectively, the negative signs implying a concave sample surface. The error in the residual stresses measured corresponding to the above error in d-spacing can also be estimated. From equation (2.06) we have,

$$\epsilon_{\phi\psi} = \frac{d_{\phi,\psi} - d_o}{d_o} = \frac{\Delta d}{d} = \frac{(1+v)}{E}\,\sigma_\phi \sin^2\psi - \frac{v}{E}(\sigma_1 + \sigma_2) \qquad (A-5)$$

Differentiating both sides of the above equation with respect to $\sin^2\psi$, we have,

$$\frac{d(\frac{\Delta d}{d})}{d(\sin^2\psi)} = \frac{(\frac{\Delta d}{d})_{\psi_2} - (\frac{\Delta d}{d})_{\psi_1}}{\sin^2\psi_2 - \sin^2\psi_1} = (\frac{1+v}{E})d\sigma_\phi \qquad (A-6)$$

In Equation (A-6), the values of the change in stress $d\sigma_\phi$ can be calculated knowing the values of $\frac{\Delta d}{d}$ from Table A-1. These calculations, done for both 7475-Al T651 and Ti-6Al-4V alloys, are shown in Table A-2. The results of Table A-2 indicate that there is no significant change in the stress values for both the sharp and blunt notches. Equations (A-1) and (A-4) are conservative

A-4

overestimates of the effect dealt with in this section. Therefore, the results of Tables A-1 and A-2 are overestimates too [34].

Table A-2. Estimate of the error in stress values for differing radius of curvature.

Radius of curvature	Material	$\Delta\sigma_\phi$ (in ksi)
3.175 mm	Al	0.95
	Ti	2.50
6.35 mm	Al	0.47
	Ti	1.23

Listing of program INTENSITY

```
C                    INTENSITY
C
C***********************************************************
C THIS IS A PROGRAM FOR INTENSITY BAND SIMULATION FROM A NOTCH SPECIMEN
C OF 7475AL-T651, FOR AN X-RAY BEAM IRRADIATING THE SURFACE OF THE
C SPECIMEN IN THE REGION BETWEEN THE NOTCHES.
C
C  INPUT PARAMETERS
C
C  D0 IS THE D-SPACING OF THE UNSTRESSED PLANES
C  ALAMDA IS THE WAVELENGTH
C  Y1 IS THE HEIGHT ABOVE THE BASE OF THE NOTCH
C  X2 IS THE POSITION ALONG THE X-AXIS
C  A(I), B(I) AND C(I) ARE THE VALUES OF THE COEFFICIENTS IN THE
C  POLYNOMIAL USED TO EXPRESS THE D-SPACING PROFILE
C  SX, SY ARE THE STRESSES IN THE X AND Y DIRECTION RESPECTIVELY
C  EX, EY, AND EZ ARE THE CORRESPONDING STRAINS
C  TT IS THE THETA VALUE CORRESPONDING TO THE D-SPACING
C  NX IS THE NUMBER OF POINTS AT WHICH STRAIN RESULTS ARE OBTAINED
C  NP IS THE TOTAL NUMBER OF POINTS GENERATED
C  SPSI IS THE SIN**2 VALUE
C  D0S, D0E, D90S, AND D90E ARE THE D-SPACING RESULTS ON SURFACE (S)
C  AND EDGE (E) RESPECTIVELY FOR PHI = 0 DEG. AN DEG. RESPECTIVELY
C  START IS THE TWO-THETA VALUE (IN DEGREES) OF THE LOW ANGLE SIDE
C  OF THE INTENSITY BAND TO BE SIMULATED
C  DELTT IS THE INCREMENT IN TWO THETA.
C***********************************************************
C
      IMPLICIT REAL*4(A-H,O-Z)
      DIMENSION D(2000),X(2000),TT(2000),X2(100)
      DIMENSION P(2000),UBP(2000),SINTEN(2000),AINTEN(2000),THETA(2000)
      DIMENSION EX(100),EY(100),EZ(100),SX(100),SY(100)
      DIMENSION D0S(50),D90S(50),D0E(50),D90E(50),SPSI(50)
      CALL FRRSET(208,256,-1)
      ALAMDA = 1.54178
      PI = ACOS(-1.0)
      RAD = 2.0*180.0/PI
C
C***********************************************************
C THE FOLLOWING ARE THE READ STATEMENTS IN THE PROGRAM.
C
      READ(5,*)D0
      READ(5,*)Y1
      READ(5,*)A1,B1,C1
      READ(5,*)A2,B2,C2
      READ(5,*)A3,B3,C3
      READ(5,*)A4,B4,C4
      READ(5,*)A5,B5,C5
C
```

```
C THE FOLLOWING ARE THE FORMAT STATEMENTS IN THE PROGRAM.
C
   1  FORMAT(/'X',8X,'SX',8X,'SY',/)
   2  FORMAT(/5X,'X2',8X,'EX',8X,'EY',8X,'EZ',/)
   3  FORMAT(/'D',8X,'X',8X,'TWO-THETA',/)
   4  FORMAT(/'TWO-THETA',8X,'INTENSITY',/)
   5  FORMAT(2X,F10.4,2(F10.3))
   6  FORMAT(2X,F10.4,3(F10.3))
   7  FORMAT(2X,F12.6,F12.4,F13.6)
   8  FORMAT(2X,F13.6,E13.6)
   9  FORMAT(2X,F5.2,4(F13.5),5X,F5.2)
  11  FORMAT(3X,'SPSI',5X,'D0SPSI',8X,'D0EPSI',7X,'D90SPSI',5X,'D90EPS
     *I',7X,'Y',/)
C********************************************************************
C
      CALL STRAIN(Y1,X2,EX,EY,EZ,SX,SY,NX)
      CALL DX2TT(D0,NX,EZ,D,TT)
      CALL DVSSIN(D0,X2,EX,EY,EZ,SPSI,D0S,D0E,D90S,D90E)
      NP = 1270
      X(1) = 0.0
C
C********************************************************************
C THE FOLLOWING DO LOOP GIVES THE SET OF EQUATIONS FOR THE D-SPACING
C CURVE FIT.
C********************************************************************
C
      DO 10 I = 1,NP
        IF(X(I).LE.0.04) D(I) = A1*(X(I)**2) + B1*X(I) + C1
        IF(X(I).GT.0.04 .AND. X(I).LE.0.08) D(I) = A2*(X(I)**2) + B2*X(I) + C2
        IF(X(I).GT.0.08 .AND. X(I).LE.0.15) D(I) = A3*(X(I)**2) + B3*X(I) + C3
        IF(X(I).GT.0.15 .AND. X(I).LE.0.21) D(I) = A4*(X(I)**2) + B4*X(I) + C4
        IF(X(I).GT.0.21 .AND. X(I).LE.0.26) D(I) = A5*(X(I)**2) + B5*X(I) + C5
        TT(I) = ASIN(ALAMDA/(D(I)*2.0))*RAD
        X(I + 1) = X(I) + 2.0E-04
  10  CONTINUE
C
C********************************************************************
C THE FOLLOWING DO LOOP CORRESPONDING TO STATEMENT # 100 GENERATES THE
C INTENSITY DUE TO EACH OF THE TEN SEGMENTS IN THE REGION BETWEEN THE
C NOTCHES
C
      N = 0
      DO 100 I = 1,10
        M = I + N
        N = N + 127
C
C LOOP 20 CALCULATES THE INTENSITY FOR EACH LAYER IN A FLAT SAMPLE
C
        DO 20 I = M,N
  20      P(I) = (X(I + 1)-X(I))/0.25
C
C INITIALISING THE UNBROADENED INTENSITY AND THE INTENSITY SIMULATED
C AT THETA(I). THETA(I) IS THE TWO-THETA POSITION AT WHICH THE
C INTENSITIES ARE TO BE SIMULATED. SINTEN IS THE INTENSITY DUE TO
C EACH SEGMENT
C
```

```
      DO 30 I = M,N
         UBP(I) = 0.0
  30  SINTEN(I) = 0.0
C
      AN = FLOAT(N)
      DELTT = 0.3/127.0
      START = TT(N) - 0.10
C
      DO 40 I = M,N
  40  THETA(I) = START + DELTT*(I-M)
C
C THE FOLLOWING LOOP CALCULATES THE INTENSITY FOR EACH POINT OF THE
C INTENSITY BAND BEING SIMULATED.
C
      DO 60 K = M,N
         IF(K.EQ.1.OR.K.EQ.NP)GO TO 108
         ALI = (THETA(K) + THETA(K-1))/2.0
         ULI = (THETA(K) + THETA(K + 1))/2.0
C
C GW AND GM ARE TWO ADJUSTABLE PARAMETERS DENOTING THE WIDTH OF THE
C GUASSIAN PEAK AND THE POWER FOR THE GUASSIAN DISTRIBUTION RESPECTIVELY
C
  108    GW = 0.01
         GM = 2.5
C
C THIS LOOP BROADENS THE CALCULATED INTENSITY OF EACH LAYER USING THE
C PEARSON VII FUNCTION. THESE ARE THEN SUPERIMPOSED TO GET THE SIMULATED
C INTENSITY.
C
      DO 50 J = M,N
         TTJ = (TT(J) + TT(J + 1))/2.0
         DIFF = THETA(K)-TTJ
         YNORM = (1.0/(SQRT(GM*PI)*GW))*(GAMMA(GM)/GAMMA(GM-0.5))
         BR = YNORM/(1.0 + (DIFF**2)/(GM*(GW**2)))**GM
         IF(K.EQ. 1.OR.K .EQ. NP)GO TO 50
         IF(TT(J).GE.ALI .AND. TT(J) .LT.ULI)UBP(K) = UBP(K) + P(J)
  50  SINTEN(K) = SINTEN(K) + P(J)*BR
  60  CONTINUE
C
C THIS WRITE LOOP WRITES THE INTENSITY VALUES DUE TO EACH OF THE TEN
C SEGMENTS ALONG WITH THEIR CORRESPONDING TWO-THETA POSITION.
C
      WRITE(6,4)
      DO 45 I = M,N
         SINTEN(I) = SINTEN(I)
         WRITE(6,8)THETA(I),SINTEN(I)
  45  CONTINUE
 100  CONTINUE
C
C*********************************************************************
C
C
C*********************************************************************
C THIS SECTION USES THE SAME PRINCIPLES AS THE PREVIOUS SECTION
C IN THE CALCULATION OF INTENSITY. THE ONLY DIFFERENCE IS THAT
C HERE THE OVERALL INTENSITY OVER THE ENTIRE DOMAIN IS CALCULATED.
```

```
C THIS OVERALL INTENSITY IS TERMED AS AINTEN.
C
      N = NP
      M = 1
      DO 120 I = M,N
 120     P(I) = (X(I + 1)-X(I))/0.25
C
      DO 130 I = M,N
         UBP(I) = 0.0
 130  AINTEN(I) = 0.0
C
      ANP = FLOAT(NP)
      DELTT = 0.3/ANP
      START = TT(N) - 0.10
C
      DO 140 I = M,N
 140  THETA(I) = START + DELTT*(I-M)
C
      DO 160 K = M,N
         IF(K.EQ.1.OR.K.EQ.NP)GO TO 1108
         ALI = (THETA(K) + THETA(K-1))/2.0
         ULI = (THETA(K) + THETA(K + 1))/2.0
C GW AND GM ARE TWO ADJUSTABLE PARAMETERS DENOTING THE WIDTH OF THE
C GUASSIAN PEAK AND THE POWER FOR THE GUASSIAN DISTRIBUTION RESPECTIVELY
 1108    GW = 0.01
         GM = 2.5
C
      DO 150 J = M,N
         TTJ = (TT(J) + TT(J + 1))/2.0
         DIFF = THETA(K)-TTJ
         YNORM = (1.0/(SQRT(GM*PI)*GW))*(GAMMA(GM)/GAMMA(GM-0.5))
         BR = YNORM/(1.0 + (DIFF**2)/(GM*(GW**2)))**GM
         IF(K.EQ. 1.OR.K .EQ. NP)GO TO 150
         IF(TT(J).GE.ALI .AND. TT(J) .LT.ULI)UBP(K) = UBP(K) + P(J)
 150  AINTEN(K) = AINTEN(K) + P(J)*BR
 160  CONTINUE
C
C THE FOLLOWING ARE THE WRITE STATEMENTS IN THE PROGRAM.
C
      WRITE(16,1)
      DO 15 I = 1,NX
         WRITE(16,5)X2(I),SX(I),SY(I)
 15   CONTINUE
      WRITE(26,2)
      DO 125 I = 1,NX
         EX(I) = EX(I)*1000.0
         EY(I) = EY(I)*1000.0
         EZ(I) = EZ(I)*1000.0
 125  CONTINUE
      DO 25 I = 1,NX
         WRITE(26,6)X2(I),EX(I),EY(I),EZ(I)
 25   CONTINUE
      WRITE(36,3)
      DO 35 I = 1,NP
         X(I) = X(I) - 0.25
         WRITE(36,7)D(I),X(I),TT(I)
```

```
   35  CONTINUE
       WRITE(46,4)
       DO 145 I = M,N
         WRITE(46,8) THETA(I),AINTEN(I)
  145  CONTINUE
       WRITE(56,11)
       DO 55 I = 1,7
         WRITE(56,9)SPSI(I),D0S(I),D0E(I),D90S(I),D90E(I)
   55  CONTINUE
C•••••••••••••••••••••••••••••••••••••••••••••••••••••••••••••••••••
C
       STOP
       END
C
C
C•••••••••••••••••••••••••••••••••••••••••••••••••••••••••••••••••••
C THIS ROUTINE CALCULATES THE D-SPACING AND THE TWO THETA VALUES FROM T
C STRAIN EZ. THIS ROUTINE CALLS THE SUBROUTINE "STRAIN" TO GET THE VALUE
C OF THE STRAIN, EZ. THIS ROUTINE ALSO CALLS ANOTHER SUBROUTINE "DPTS"
C WHICH IS USED TO FIT A CURVE THROUGH THE POINTS OF D VS X GENERATED
C IN SUBROUTINE "DX2TT".
C•••••••••••••••••••••••••••••••••••••••••••••••••••••••••••••••••••
       SUBROUTINE DX2TT(D0,NX,EZ,D,TT)
       DIMENSION EX(100),EY(100),EZ(100),D(2000),TT(2000)
C     IMPLICIT REAL*4(A-H,O-Z)
       PI = ACOS(-1.0)
       RAD = 2.0*180.0/PI
       ALAMDA = 1.54178
       D0 = 2.0235
       DO 100 I = 1,NX
         D(I) = (1.0 + EZ(I))*D0
         TT(I) = ASIN(ALAMDA/(D(I)*2.0))*RAD
  100  CONTINUE
       RETURN
       END
C
C•••••••••••••••••••••••••••••••••••••••••••••••••••••••••••••••••••
C   THIS ROUTINE CALCULATES THE D-SPACING VALUES AT THE NOTCH TIP FOR
C   DIFFRENT VALUES OF PSI, FOR BOTH SURFACE AND EDGE. THESE VALUES
C   CAN BE GENERATED FOR ANY POSITION ALONG THE X-AXIS, BUT FOR
C   VERIFICATION, THE VALUES AT THE NOTCH TIP ARE GIVEN HERE.
C•••••••••••••••••••••••••••••••••••••••••••••••••••••••••••••••••••
C
       SUBROUTINE DVSSIN(D0,X2,EX,EY,EZ,SPSI,D0S,D0E,D90S,D90E)
       DIMENSION X2(100),EX(100),EY(100),EZ(100),SPSI(50)
       DIMENSION D0S(50),D90S(50),D0E(50),D90E(50)
         PI = ACOS(-1.)
         PSI = 0.0
         J = 1
         DO 20 I = 1,7
           PHI = 0.0
           SPHI = SIN(PHI)**2
           CPHI = COS(PHI)**2
           D0S(I) = D0*(1.0 + EZ(J) + (EX(J)*CPHI + EY(J)*SPHI-EZ(J))
      *        *(SIN(PSI)**2))
           D0E(I) = D0*(1.0 + EX(J) + (EY(J)*CPHI + EZ(J)*SPHI-EX(J))
```

```
     *      *(SIN(PSI)**2))
            PHI = 90.0*PI/180.
            SPHI = SIN(PHI)**2
            CPHI = COS(PHI)**2
            D90S(I) = D0*(1.0 + EZ(J) + (EX(J)*CPHI + EY(J)*SPHI-EZ(J))
     *      *(SIN(PSI)**2))
            D90E(I) = D0*(1.0 + EX(J) + (EY(J)*CPHI + EZ(J)*SPHI-EX(J))
     *      *(SIN(PSI)**2))
            SPSI(I) = SIN(PSI)**2
            PSI = PSI + 15.0*ACOS(-1.0)/180.0
  20     CONTINUE
       RETURN
       END
C
C******************************************************************
C    THIS SUBROUTINE CALCULATES THE STRESS AND STRAIN VALUES IN THE X
C    AND Y DIRECTION AS A FUNCTION OF THE DISTANCE BETWEEN NOTCHES.
C    THE STRAIN VALUES, THE TOTAL NUMBER OF POINTS ALONG THE X DIREC-
C    TION AND THE CORRESPONDING X AND Y VALUES ARE THEN RETURNED TO
C    THE MAIN PROGRAM FOR GENERATING THE D-SPACING PROFILE.
C******************************************************************
C
       SUBROUTINE STRAIN(Y1,X2,EX,EY,EZ,SX,SY,NX)
C    IMPLICIT REAL*8(A-H,O-Z)
       DIMENSION EX(100),EY(100),EZ(100),
      1 SX(100),SY(100),TXY(100),X1(100),X2(100)
       E = 10300.0
       PNU = 1.0/3.0
       T = 0.342
       A = 0.250
       RHO = 0.125
       V0 = ATAN(SQRT(A/RHO))
C
C    E IS THE YOUNG'S MODULUS OF THE MATERIAL.
C    PNU IS THE POISSON'S RATIO.
C    T IS THE THICKNESS OF THE SPECIMEN.
C    A IS HALF THE DISTANCE BETWEEN NOTCHES.
C    RHO IS THE NOTCH ROOT RADIUS OF CURVATURE.
C    V0 IS THE HYPERBOLA PARAMETER.
C
       S = 70.0
C    S = P/(2*A*T)
C    SA = 35.0
       C1 = SIN(V0)
       C2 = COS(V0)
       CA = S*C1/(V0 + C1*C2)
C
C    S IS THE NOMINAL STRESS FOR THE LOAD P.
C    SA IS THE STRESS AMPLITUDE WHICH IS S/2.
C    CA IS A CONSSTANT WITH THE DIMENSIONS OF STRESS.
C    C IS A SCALING FACTOR USED IN THE STRESS DISTRIBUTION EQUATIONS.
C    Y1 = SINH(U)*COS(V)
C    X1 = X/C = COSH(U)*SIN(V)
C    U AND V ARE THE CURVILINEAR COORDINATES.
C
```

```
       C = A/C1
C      THE FOLLOWING IF LOOP CALCULATES THE STRESS VALUES IN THE X AND
C      Y DIRECTIONS, SX AND SY, SHEAR STRESS TXY AND THE CORRESPONDING
C      STRAIN VALUES EX, EY AND EZ. AS A FUNCTION OF THE LINE ALONG THE
C      BASE OF THE NOTCHES. THE VALUES ARE FIRST DERIVED IN CURVILINEAR
C      COORDINATES AND A COORDINATE TRANSFORMATION IS USED TO CONVERT TO
C      CARTESIAN COORDINATES.
C      X-MAX IS THE MAXIMUM VALUE ON THE HYPERBOLA.
C      X-MIN AND XX-MIN ARE THE MINIMUM VALUES ON THE HYPERBOLA.
C      H IS THE FACTOR OF DISTORTION FOR THE HYPERBOLA.
C
       U1 = ALOG(Y1/C2 + SQRT((Y1/C2)**2 + 1))
       XXMIN = -C*COSH(U1)*SIN(V0)
       XMAX = C*COSH(U1)*SIN(V0)
       XMIN = XXMIN
       NX = 0
       X2(1) = XMIN
       J = 0
  20   J = J + 1
       X1(J) = XMIN/C
       Q1 = 1.0 + (X1(J)**2) + (Y1**2)
       Q = SQRT((Q1-SQRT(Q1**2-4.0*(X1(J)**2)))/2.0)
       V = ASIN(Q)
       U = ALOG(Y1/COS(V) + SQRT((Y1/COS(V))**2 + 1.0))
       H = SQRT((Y1**2)/COS(V)**2 + COS(V)**2)
       SU = CA*COSH(U)*COS(V)*(2.0*(H**2) + COS(V0)**2-COS(V)**2)/H**4
       SV = CA*COSH(U)*COS(V)*(COS(V)**2-COS(V0)**2)/H**4
       TUV = CA*SINH(U)*SIN(V)*(COS(V0)**2-COS(V)**2)/H**4
       ALPHA = ACOS(C/H*COSH(U)*COS(V))
       SX(J) = (SU + SV)/2.0 + (SU-SV)*COS(2*ALPHA)/2.0-TUV*SIN(2*ALPHA)
       SY(J) = (SU + SV)/2.0-(SU-SV)*COS(2*ALPHA)/2.0 + TUV*SIN(2*ALPHA)
       TXY(J) = (SU-SV)*SIN(2*ALPHA)/2.0 + TUV*COS(2*ALPHA)
C
C THE FOLLOWING ARE THE CORRESPONDING ELASTIC STRAINS.
C
       EX(J) = (SX(J)-PNU*SY(J))/E
       EY(J) = (SY(J)-PNU*SX(J))/E
       EZ(J) = -(SX(J) + SY(J))*PNU/E
C      S1 = (SX(J) + SY(J))/2.0 + SQRT(((SX(J)-SY(J))**2)/4.0 + TXY(J)**2)
C      S1 = (SX(J) + SY(J))/2.0-SQRT(((SX(J)-SY(J))**2)/4.0 + TXY(J)**2)
       NX = NX + 1
       XMIN = XMIN + (XMAX-XXMIN)/50.0
       K = J + 1
       X2(K) = XMIN
       IF(XMIN.LE.0.26)GO TO 20
       RETURN
       END
```

Sample input files

```
C
C    Input file for (200) plane
C
    2.0235          (d_e)
    0.00                  (y_1)
    -0.5                  (a_1)
    0.067       (b_1)
    2.01441     (c_1)
    -0.175
    0.0435
    2.01483
    -0.063
    0.0254
    2.01556
    -0.03333333
    0.01633333
    2.01625
    -0.025
    0.0125
    2.0166875
C
C    Input file for (400) plane
C
    1.01175
    0.00
    -0.25
    0.0335
    1.00721
    -0.0625
    0.01875
    1.0075
    -0.03333333
    0.013
    1.0077733
    -0.01666667
    0.00817
    1.0081229
    -0.01
    0.0053
    1.00843
C
C    Input file for (333) plane
C
    0.7788455
    0.00
    -0.1731
    0.025
    0.77534771
    -0.0656
    0.0165
    0.7755154
    -0.0259
    0.01
```

0.7757831
-0.0138
0.006632
0.7760245
-0.011
0.005495
0.7761397

Output generated

```
C*********************************************************************
C
C  THE OUTPUT THAT CAN BE GENERATED FROM THE PROGRAM ARE
C
C     1) STRESS VALUES IN THE X & Y DIRECTIONS VARYING ALONG X.
C        THESE CAN BE OBTAINED FOR DIFFERENT HEIGHTS ALONG Y.
C     2) STRAINS IN THE X, Y AND Z DIRECTIONS.
C     3) D-SPACING VALUES CORRESPONDING TO THE STRAIN EZ.
C     4) BROADENED INTENSITY PROFILE FROM THE D-SPACING GRADIENT.
C     5) INTENSITY PROFILES FROM TEN SEGMENTS DUE TO PARTIAL
C        SUMMATION.
C
C*********************************************************************
```

Northrop Corporation
Attn: Dr. Ratwani
One Northrop Avenue
Hawthorne, CA   90250   1 copy

Northrop Corporation
Attn: Mr. Alan Liu
One Northrop Avenue
Hawthorne, CA   90250   1 copy

Rockwell International Science Center
Attn: Dr. F. Morris
1049 Camino Dos Rios
Thousand Oaks, CA   91360   1 copy

University of Dayton Research Institute
Attn: Dr. Gallagher
300 College Park Avenue
Dayton, OH   45469   1 copy

LTV Aerospace and Defense Company
Attn: Dr. C. Dumesnil
P.O. Box 225907
Dallas, TX   75265-0003   1 copy

University of Oklahoma
School of Aerospace, Mechanical
   and Nuclear Engineering
Attn: Dr. D. M. Egle
Norman, OK   78301   1 copy

LTV Aerospace and Defense Company
Attn: Mr. T. Gray
P.O. Box 225907
Dallas, TX 75265-0003   1 copy

Boeing Commercial Airplane Company
Attn: Mr. Porter
P.O. Box 3707
Seattle, WA 98124   1 copy

Fairchild Industries
Attn: Technical Library
Hagerstown, MD 21740   1 copy

Grumman Aerospace Corporation
Attn: Dr. H. Armen
South Oyster Bay Road
Bethpage, LI, NY 11714   1 copy

Lehigh University
Attn: Dr. Sih
Institute of Fracture & Solid Mechanics
Bethlehem, PA 18015   1 copy

Lehigh University
Attn: Dr. T. J. Delph
Institute of Fracture & Solid Mechanics
Bethlehem, PA 18015   1 copy

McDonnell Douglas Corporation
Attn: Mr. D. Rich
P. O. Box 516
St. Louis, MO 63166   1 copy

Northrop Corporation
Attn: Mr. A. Liu
One Northrop Avenue
Hawthorne, CA 90250   1 copy

Rockwell International Corporation
Attn: Mr. J. Chang
LA Division/International Airport
P.O. Box 92098
Los Angeles, CA 90009   1 copy

Sikorsky Aircraft
Attn: S. Garbo
110 N. Main Street
Stratford, CT 06622   1 copy

University of Illinois
College of Engineering
Attn: Professor D. Socie
Urbana, IL 61801   1 copy

University of Pennsylvania
Department of Mechanical Engineering
Attn: Dr. Burgers
111 Towne Bldg., D3
Philadelphia, PA 19104   1 copy

Rockwell International Corporation
Attn: Mr. F. Kaufman
4300 East Fifth Avenue
Columbus, OH 43216   1 copy

Rohr Corporation
Attn: Dr. F. Riel
Riverside, CA 92503   1 copy

Boeing Helicopter Company
Attn: C. Gunther
P.O. Box 16858
Philadelphia, PA   19142   1 copy

Douglas Aircraft Company
Attn: Mr. Luce (7-21)
3855 Lakewood Blvd.
Long Beach, CA   90846   1 copy

General Dynamics/Convair
Attn: Mr. G. Kruse
P.O. Box 80847
San Diego, CA   92138   1 copy

Grumman Aerospace Corporation
Attn: Dr. B. Leftheris
South Oyster Bay Road
Bethpage, LI, NY   11714   1 copy

Lehigh University
Attn: Prof. R. Wei
Institute of Fracture & Solid Mechanics
Bethlehem, PA   18015   1 copy

Lockheed Aeronautical Systems Co. - Georgia
Attn: Mr. T. Adams
86 S. Cobb Drive
Marietta, GA   30063   1 copy

Lockheed Aeronautical Systems Co. - Georgia
Attn: M. B. M. Shah
86 S. Cobb Drive
Marietta, GA   30063   1 copy

National Aeronautical & Space Adm
George C. Marshall Space Flight Ctr
Attn: Technical Library
Huntsville, AL 35812   1 copy

National Aeronautical & Space Adm
Lewis Research Center
Attn: Technical Library
Cleveland, OH 44135   1 copy

Air Force Systems Command
Attn: AFWAL/FDS
Wright Patterson Air Force Base
OH 45433   1 copy

Air Force Systems Command
Attn: AFWAL/FDSA
Wright Patterson Air Force Base
OH 45433   1 copy

Air Force Systems Command
Attn: AFWAL/FDSE
Wright Patterson Air Force Base
OH 45433   1 copy

ALCOA
ALCOA Labs
Attn: Mr. J. G. Kaufman
ALCOA Center, PA 15069   1 copy

Bell Helicopter Company
Textron Inc.
Attn: T. Haas
P.O. Box 482
Ft. Worth, TX 76101   1 copy

Boeing Helicopter Company
Attn: W. Kesack
P.O. Box 16858
Philadelphia, PA 19142   1 copy

```
General Dynamics Corporation
Attn: Dr. S. Manning
P.O. Box 748
Ft. Worth, TX  76101                          1 copy


Grumman Aerospace Corporation
Attn: H. Eidenoff
South Oyster Bay Road
Bethpage, LI  NY  11714                        1 copy


Lockheed Aeronautical Systems Company
Attn: Mr. J. Ekvall/76-23, Bldg. 63
P. O. Box 551
Burbank, CA  91520                             1 copy


Lockheed Aeronautical Systems Company
Attn:  Mr. E. Walker/76-23, Bldg. 63
P.O. Box 551
Burbank, CA  91520                             1 copy


McDonnell Aircraft Company
McDonnell Douglas Corporation
Attn: R. Pinckert
P.O. Box 516
St. Louis, MO  63166                           1 copy


Federal Aviation Administration
800 Independence Avenue, SW
(Attn:  Mr. J. Soderquist)
Washington, D.C.  20591                        1 copy


National Aeronautics & Space Adm
Langley Research Center
Attn:  Mr. C. E. Harris/MS188E
Hampton, VA  23365                             1 copy
```

Army Materials Technology Laboratory
Attn: D. Oplinger/SLCMT-MS
Watertown, MA 02172-0001   1 copy

National Technical Information Center
U. S. Department of Commerce
Springfield, VA 221512   2 copy

Oklahoma City Air Logistics Center
Attn: MAQCP
Tinker Air Force Base
Oklahoma 73145   1 copy

United States Army
Research Office
Durham, NC 27701   1 copy

Defense Technical Information Center
Attn: Administrator
Building #5, Cameron Station
Alexandria, VA 22314   2 copies

U.S. Army R&D Center
Attn: STRBE-VC/L. Ryan
Fort Belvoir, VA 22060-5606   1 copy

Battelle Columbus Laboratories
Attn: Dr. B. Leis
505 King Avenue
Columbus, OH 43201   1 copy

Drexel University
Attn: Dr. Auerbuch
32nd and Chestnut Streets
Philadelphia, PA 19104   1 copy

Director
Naval Research Laboratory
Attn: Dr. R. Badaliance
Washington, DC   20375   1 copy

Sacramento Air Logistics Center
Attn: MANE/A. J. Hammond
McClellan Air Force Base
Sacramento, CA   95652   1 copy

Metals and Ceramics Information Ctr
Battelle Columbus Laboratories
505 King Avenue
Columbus, OH   43201   1 copy

Warner-Robbins Air Logistics Ctr
Attn: MMSRD/Mr. T. Christian
Robins Air Force Base
Georgia   30198   1 copy

Army Applied Technology Directorate
U.S. Army Aviation Research & Technology Activity
Attn: SAVRT-TY/H. Reddick
Fort Eustis, VA   23604-5577   1 copy

Ogden Air Logistics Center
Attn: MANCC
Hill Air Force Base
Utah 84055   1 copy

San Antonio Air Logistics Center
Attn: MMETM
Kelly Air Force Base
San Antonio, TX   78241   1 copy

NASA Headquarters
Attn: Dr. D. Mulville
OAST-Code RM
Washington, D.C.   20546   1 copy

Commander
Naval Air Engineering Center
Attn: Mr. F. Sinatra
Lakehurst, NJ   08733   1 copy

Commander
Naval Air Engineering Center
Attn: Mr. Neil Goodis
Lakehurst, NJ   08733   1 copy

Commanding Officer
Naval Aviation Depot
Attn: Technical Library
Marine Corps Air Station
Cherry Point, NC   28533-5030   1 copy

Commanding Officer
Naval Aviation Depot
Attn: Technical Library
North Island
San Diego, CA   92135   1 copy

Commander
Naval Aviation Depot Operations Center
Patuxent River, MD   20670   1 copy

Commander
David Taylor Research Center
Attn: Technical Library
Bethesda, MD   20034   1 copy

```
Commanding Officer
Naval Air Systems Command
Attn: AIR-530
Washington, D.C.   20361                    3 copies


Commanding Officer
Naval Air Systems Command
Attn: AIR-5302
Washington, D.C.   20361                    1 copy


Commanding Officer
Naval Air Systems Command
Attn: AIR-53021
Washington, D.C.   20361                    1 copy


Commanding Officer
Naval Air Systems Command
Attn: AIR-53022
Washington, D.C.   20361                    1 copy


Commanding Officer
Naval Air Systems Command
Attn: AIR-53023
Washington, D.C.   20361                    1 copy


Federal Aviation Administration
Technical Center
Attn:  Mr. L. Neri, Code ACT-330
Atlantic City, NJ  08405                     1 copy


Federal Aviation Administration
Technical Center
Attn:  Mr. M. Ciafa, Code ACT-330
Atlantic City, NJ  08405                     1 copy
```

Commanding Officer
Naval Aviation Depot
Attn: Technical Library
Jacksonville, FL 32212   1 copy

Commanding Officer
Naval Aviation Depot
Attn: Technical Library
Pensacola, FL 32508   1 copy

Commander
Naval Post Graduate School
Attn: Prof. K. Challenger
Monterey, CA 95940   1 copy

Officer in Charge
David Taylor Research Center
Attn: 2814/T. Montemarano
Annapolis, MD 21402   1 copy

Naval Surface Weapons Center
White Oak Laboratory
Attn: Technical Library
Silver Spring, MD 20910   1 copy

Commanding Officer
Naval Air Systems Command
Attn: AIR-00D4
Washington, D.C. 20361   1 copy

Commanding Officer
Naval Air Systems Command
Attn: AIR-931B
Washington, D.C. 20361   1 copy

NAVAIRDEVCEN
Attn: Code 8131
Warminster, PA 18974-5000   2 copies

DISTRIBUTION LIST

REPORT NO. NADC-88141-60

Commander
Naval Air Test Center
Attn: Dr. J. Hoeg
Patuxent River, MD 20670   1 copy

Commanding Officer
Naval Aviation Depot
Attn: Technical Library
Alameda, CA 94501   1 copy

Commanding Officer
Naval Aviation Depot
Attn: Mr. H. Stokley
Norfolk, VA 23511-5899   1 copy

Commander
Naval Weapons Center
Attn: J. Morrow, Code 338
China Lake, CA 93555   1 copy

Naval Sea Systems Command
Attn: SEA-05R
Washington, D.C. 20362-5101   1 copy

Office of Naval Research
Attn: Dr. Rajapakse, Code 11325M
800 North Quincy Street
Arlington, VA 22217   1 copy

Office of Naval Technology
Attn: Capt. K. Cox, ONT-21
800 North Quincy Street
Arlington, VA 22217   1 copy

Center for Naval Analyses
4401 Font Avenue
P.O. Box 16268
Alexandria, VA 22302-0268   1 copy